

# Eruptive transition and vent activity during lava fountains at Etna volcano revealed by integrated remote sensing

Francesco Amadio<sup>\*α</sup>, Luigi Mereu<sup>β</sup>, Emilio Pecora<sup>β</sup>, Simona Scollo<sup>β</sup>, Giulio Vignoli<sup>α</sup>, and Laura Pioli<sup>α</sup>

<sup>α</sup> Dipartimento di Scienze Chimiche e Geologiche, Università di Cagliari, Cittadella Universitaria, Monserrato 09042, Italy.

<sup>β</sup> Istituto Nazionale di Geofisica e Vulcanologia, Osservatorio Etno, Piazza Roma 2, 95125 Catania, Italy.

## ABSTRACT

Paroxysmal mafic activity is a relevant source of hazard at many active volcanoes. At volcanoes like Etna (Italy), paroxysmal eruptions have highly variable transient dynamics, thus monitoring activities are crucial for the understanding and quantification of the onset of climactic phases. We examined thermal videos from the INGV-OE (Istituto Nazionale di Geofisica e Vulcanologia – Osservatorio Etno) monitoring network of seven lava fountains that occurred at the South-East Crater in 2021. We identified the processes that precede and lead to the onset of the fountaining phase to implement a thermal analysis tool that can be used, in conjunction with radar data, to fully characterize the dynamics and duration of paroxysmal events. Based on the signal derived by our parameter, we recognized different phases (Strombolian; waxing; waning) preceding and following the climax of the paroxysms. Our method, if linked with other monitoring data, could also be easily implemented in early warning systems.

**KEYWORDS:** Eruption dynamics; Vent opening; Thermal monitoring; Radar monitoring.

## 1 INTRODUCTION

Open-conduit basaltic volcanoes are typically characterized by persistent gas emission and variable explosive behaviour, posing hazards that depend on the prevailing eruptive style. While often associated with mild activity, mafic systems are also capable of more energetic explosions, such as high lava fountains or violent Strombolian eruptions [Swanson et al. 2014; Taddeucci et al. 2015a; Edwards et al. 2018; Trusdell et al. 2019], as observed at many volcanoes around the world such as Villarrica (Chile) [Johnson et al. 2018]; Yasur (Vanuatu), [Simons et al. 2020b], Stromboli (Italy) [Bertagnini et al. 2011; Métrich et al. 2021], Etna (Italy) [Vicarò et al. 2019; Andronico et al. 2021], Fuego (Guatemala) [Naismith et al. 2019; Liu et al. 2020], and Santiaguito (Guatemala) [Williams-Jones and Rymer 2015]. This more energetic activity is typically transient and often happens with little to no warning, as seen during the 2015 paroxysm at Villarrica volcano [Aiuppa et al. 2017; Johnson et al. 2018].

Paroxysmal eruptions at mafic volcanoes consist of high-energy lava fountains that rise from tens to hundreds of meters above the active crater and can last for tens of minutes to a few days [Taddeucci et al. 2015b]. This activity leads to the formation of a gas and ash-rich column that can rise up to 10–15 km a.s.l. and drift for dozens of kilometres away from the active crater posing a serious threat to local communities and air traffic [Blong 1984; Casadevall 1994; Guffanti et al. 2009; Mereu et al. 2025].

Early models of lava fountaining discussed the role of magma degassing and distinct flow processes occurring either in the conduit or within the magma reservoir in driving the eruption [Wilson and Head 1981; Jaupart and Vergnolle 1989]. Relatively high magma viscosity can also significantly increase eruption explosivity [Houghton et al. 2004; Gonnermann and

Manga 2007], but it hardly explains the dynamics of paroxysmal events [Calvari and Nunnari 2022]. A comprehensive model describing the critical processes triggering paroxysmal mafic explosive events has not yet been proposed, possibly due to the lack of high-resolution datasets on a statistically significant number of events that occurred at different volcanoes. Such data could clarify the relative role of magma supply rates, magma composition, and the shallow magma transport structures (i.e., reservoir and conduit geometry) in controlling the fluid dynamics that drive these explosive eruptions.

Existing datasets derive from both classical field studies [Alparone et al. 2007; Scollo et al. 2008; Costantini et al. 2011; Romero et al. 2018; Simons et al. 2020a; Amadio et al. 2024] and from real-time monitoring, involving the acquisition and processing of various types of data (i.e., seismic, infrasound, deformation signals, gas and tephra geochemistry, atmospheric [Alparone et al. 2003; Aiuppa et al. 2008; Bonaccorso et al. 2013; Ripepe et al. 2018; Queißer et al. 2019; Spampinato et al. 2019; Corsaro and Miraglia 2022]). Furthermore, monitoring active volcanic areas is crucial to better understand eruption processes. Early recognition of hazardous behaviour is critical to reducing the risk associated with an eruptive event [Tilling 1987; Andronico et al. 2005; Sparks et al. 2012; Pallister and McNutt 2015; Corsaro et al. 2017; Newhall et al. 2017; Coppola et al. 2020].

Thermal monitoring is currently one of the most effective monitoring tools, capable to provide important eruptive parameter in near-real time. For example, a combination of fixed thermal-infrared (TIR) cameras, handheld radiometers, and UAS (Unoccupied Aerial System)-mounted TIR sensors can produce high-cadence surface-temperature maps that resolve rapid changes in vents and lava flow fields often missed by satellites [Sansivero and Vilardo 2019]. These systems require rigorous radiometric calibration and atmospheric and emissivity correction to derive quantitative temperatures or

\*✉ francesco.amadio@unica.it

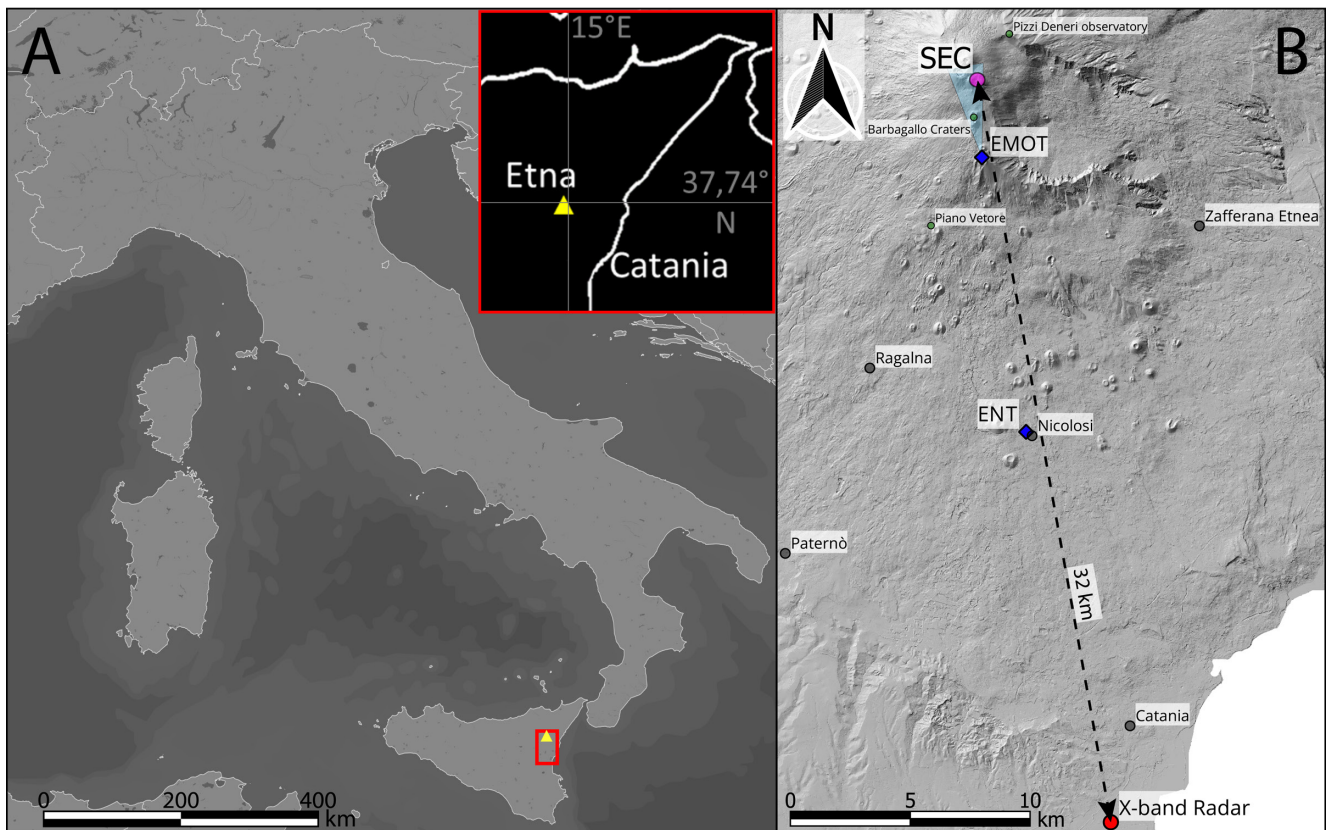


Figure 1: [A] Map showing the position of Etna within Italy and [B] DTM Map of the Middle East of Sicily showing the position of the instrumentation used in this work (EMOT and ENT thermal cameras blue diamonds; X-band weather radar red circle), with respect to the South-East Crater (magenta circle). Gray and green circles are representing the main cities and sites of interest around Etna respectively. Cyan area is representing the field of view of EMOT thermal camera.

areas [Prata et al. 2024]. Volcanic radiant power (VRP) can be retrieved from calibrated TIR time-series. Empirical or physics-based conversions of VRP to time-averaged discharge rates (TADR) and erupted volumes are now standard practice when flow geometry and thermal losses are constrained [Harris and Baloga 2009]. Moreover, UAS-based TIR surveys yield sub-meter thermal mapping that, when fused with high resolution DEMs, allow mapping of lava flow and tephra deposits [Carr et al. 2021].

At Etna, fixed TIR cameras have been used to measure fountain heights, to map evolving flow fronts and produce VRP time-series that, when integrated with other monitoring data, enable near-real-time estimates of effusion rates, erupted volumes [Calvari and Nunnari 2022], and timely volume estimates for a rapid hazard assessment [Proietti et al. 2023]. In this study, we analyse thermal videos from the INGV-OE (Istituto Nazionale di Geofisica e Vulcanologia – Osservatorio Etneo) monitoring network of a series of paroxysmal events that occurred in 2021 on the South-East Crater (SEC) of Etna volcano (Figure 1). We correlate the thermal signal to the weather radar data obtained by the Italian Civil Protection Department (DPC) to find precursors of the climactic phase of paroxysms. Thermal and visual recordings, when integrated with atmospheric data from weather radar, can provide insight on the characteristic and dynamics of the eruptive event and formation of the associated plume. Some of the events un-

der consideration occurred within a few days of each other, or even within hours of a previous eruptive event (INGV-OE reports available on [www.ct.ingv.it](http://www.ct.ingv.it)). Etna provides an ideal natural laboratory for this analysis due to its frequent summit activity and dense monitoring network.

Etna displays highly variable and often complex eruptive behavior. It alternates periods in which activity occurs either in single summit crater (e.g. August–December 2006 [Andronico et al. 2014]; February–April 2021 [Amadio et al. 2024]), or in multiple craters (e.g. 2011–2013 [Viccaro et al. 2015]; the 2016 event [Edwards et al. 2018; Edwards and Pioli 2019]). A series of paroxysmal events, with periods of repose that range from a few days to weeks in duration, can also occur [Bonaccorso et al. 2021; Calvari et al. 2021]. The increase in frequency of paroxysmal eruptions over the last 20 years has significantly increased the hazard associated with explosive activity at Etna.

Within a paroxysmal episode Strombolian activity typically evolves into a lava fountain that forms ash-rich plumes, with heights ranging between 6 up to 12 km a.s.l. [Mereu et al. 2020]. Lava fountains are also frequently accompanied by lava flows [Alparone et al. 2003; Polacci et al. 2006]. Identifying when such transitions take place is critical for improving hazard assessment.

In this paper we explore the dynamics and processes that lead to the onset and cessation of the lava fountain to better understand the transient dynamics of paroxysmal events. The

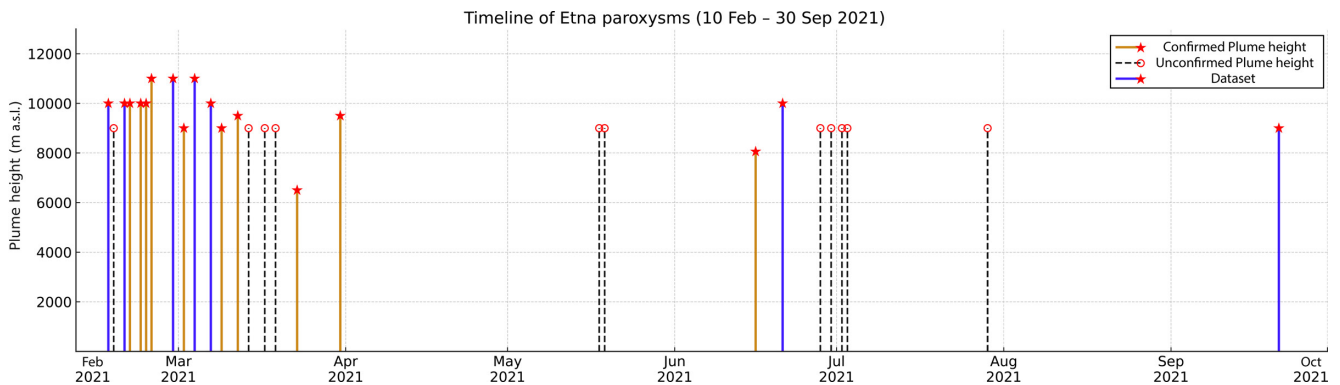


Figure 2: Timeline of Etna paroxysmal eruption from February to October, with plume height on the Y axis. Events for which the plume height is confirmed by multiple geophysical and visual observations (e.g. radar or cameras) are highlighted with solid lines and red stars, where the plume height is unconfirmed, the eruption is highlighted by black dashed lines and red circles. Solid blue lines represent eruptions studied in this paper; solid yellow lines are not described in this study.

aim of this research was to better understand the evolution from Strombolian activity to lava fountaining by exploring the transition between these phases.

## 2 ERUPTION DATABASE AND METHODS

The seven eruptive events analysed in this paper (P1 to P7; [Table 1](#) and [Figure 2](#)) are part of the Etna eruptive crisis that began in December 2020 and ended in February 2022, in which 62 paroxysmal eruptions occurred from the SEC [[Calvari and Nunnari 2022](#); [Giuffrida et al. 2023](#)]. The most intense phase of this crisis occurred between February and April 2021, when 17 eruptive events occurred within only a few days of each other, followed by about a month and a half of inactivity. Eruptive activity resumed in mid-April and continued until July 2021. From this time, sporadic eruptions alternated with periods of inactivity ranging in duration from 20 days to a month and a half until the end of the eruptive crisis [[Andronico et al. 2021](#); [Calvari and Nunnari 2022](#); [Giuffrida et al. 2023](#)].

Given the extensive network of the INGV-OE monitoring system, it was possible to study some of these events based on a multidisciplinary approach combining thermal signals with radar-based retrievals. The studied eruptions were chosen based on radar measurement availability and on their visibil-

Table 1: This table shows the date of the analysed eruptions. Starting time, ending time, and duration of lava fountains are from [Calvari and Nunnari \[2022\]](#). The investigation period refers to the piece of video analysed which comprises the entire eruption event. Time is expressed in UTC.

N°	Date	Start	End	Duration (min)	Investigated period
P1	16/02/2021	16:11	17:02	51	14:00–19:00
P2	19/02/2021	08:16	10:06	110	07:00–12:00
P3	28/02/2021	07:31	08:34	63	06:50–09:25
P4	04/03/2021	07:11	09:32	141	05:00–11:00
P5	07/03/2021	04:10	07:01	171	01:00–08:00
P6	24/06/2021	09:45	10:26	41	07:30–12:30
P7	21/09/2021	07:21	08:35	74	05:00–10:00

ity from thermal and visible cameras of the INGV-OE monitoring network; they mostly occurred during daylight and under favourable weather conditions (little or no cloud covering). Each eruptive episode included one to five hours of pre- and one hour of post-climactic activity to fully include Strombolian activity and post-eruption behaviours. Changes in time interval analysed are due to logistic or technical issues. As example, in the case of eruption P4, whose pre climactic activity (i.e., Strombolian bursts) lasted for about seven hours with no significant changes, we decided to start the thermal analysis including only the last three hours preceding the climax of the lava fountain. An exception to the set rule is the study of the P3 eruption, which started only one hour before the onset of the paroxysmal phases, due to technical issues of the camera system ([Table 1](#)).

### 2.1 Sensor network

The INGV-OE video monitoring network is equipped with fourteen fixed cameras, five operating in the infrared and nine in the visible wavelengths. To standardize the analyses, we chose to implement our tool on the camera located at La Montagnola crater ([Figure 1](#), Station ID: EMOT). It is equipped with a FLIR A655 camera that records in the 7.5–14  $\mu\text{m}$  spectral range, providing  $640 \times 480$  pixel (px) images with a spatial resolution of the summit area of about  $2.1 \text{ m px}^{-1}$ , a field of view per pixel (IFOV) of  $0.68 \mu\text{rad}$  and recording at 1 frame per second (fps). The FLIR A655 has thermal sensitivities of 30 mK at  $30^\circ\text{C}$ . EMOT thermal images are displayed with a fixed colour scale that ranges between  $-40$  and  $150^\circ\text{C}$ . We also used the thermal-infrared camera located at about 15 km ([Figure 1](#), Station ID: ENT) south from the Etna summit craters. ENT provides a time series of  $640 \times 480$  pixel images with the same camera as EMOT, imaging the summit area with a resolution of about  $10 \text{ m px}^{-1}$ . The images are displayed with a fixed colour scale with a range of  $-10$  to  $70^\circ\text{C}$  [[Calvari et al. 2011](#); [Bonaccorso et al. 2014](#)]. The ENT camera was used to estimate the maximum height of the lava fountain jet, which can be detected by selecting the saturated portion of the measured brightness frame of ENT. The brightness temperature saturation depends on the properties of the camera and on

environmental factors (methodologies in Mereu et al. [2020]). This research focused on the analysis of thermal .png images, routinely collected and saved in real time during monitoring procedures. They are saved in INGV data repositories, thus retrievable also for past eruptions.

Generally, Etna events can be observed and monitored using dual-polarization scanning weather radar operating at X-band (9.6 GHz), located at the V. Bellini airport in Catania, approximately 32 km from the Etna summit (Figure 1B). This radar performs a 3D-scan of the surrounding area (azimuth, range and elevation) within a time frame of a few minutes [Vulpiani et al. 2016; Mereu et al. 2022]. We focus on the information that the EMOT camera gives us about the dynamics of these eruptions, highlighting the main processes and evaluating their possible correlation with radar-derived Eruption Source Parameters (ESPs [Mastin et al. 2009]) estimations. The main goal was to explore the ability of real-time thermal monitoring in providing quantitative data that could be used to describe eruptive behaviour and detect transition to paroxysmal eruptions.

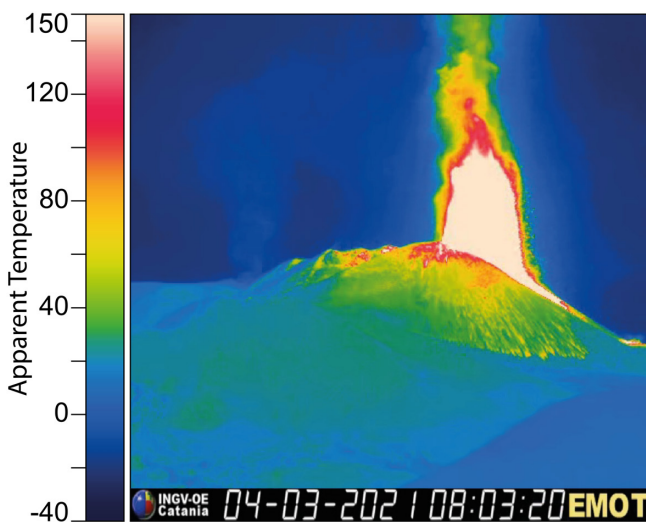


Figure 3: A frame of EMOT and its colour palette, with apparent temperatures range between  $-40$  and  $150$  °C. Time is expressed in UTC.

## 2.2 Thermal imaging collection and analyses

During routine monitoring, thermal data are converted into .png radiometric RGB (Red, Green, and Blue) images at a frequency of 1 fps. These images are then compiled into 5-minute .avi movie files, which are saved in a repository and accessible anytime for monitoring purposes or further analyses. The radiometric RGB images are generated based on a defined colour palette which extends throughout the range of apparent temperatures ( $-40$  to  $150$  °C; Figure 3). In other words, each pixel is assigned a palette colour which corresponds to a definite apparent temperature. To recover a thermal signal from .png images, we converted assigned colours to apparent temperature ( $AT$ ) according to the original palette and the temperature range (Figure 3).

For each frame, the apparent temperature was averaged across a selected area of interest. We selected:

1. Single vent areas (areas of  $100 \text{ px}^2$ ,  $10 \times 10 \text{ px}$ ); small square areas were placed directly above the active vents; due to variability of vent position within the SEC, these Areas of Interest (AOI) were manually adjusted for each analysed event (Figure 4A). Single vent data were also averaged from multiple vent regions (Multiple area, MA signal) to assess how individual vent behaviour relates to overall eruption dynamics (Figure 6B).
2. Single large area (SA signal, one study area,  $400 \times 310 \text{ px}$ ) positioned above the SEC. We opted for an area of this size to best capture the entire eruptive jet. This area covers the entire SEC crater and also captures eruptions driven by vents located outside the central sector (see Section 3.1). For this reason, we were able to use the same area for all eruptions (Figure 4B).

To reduce high-frequency oscillations, primarily caused by turbulent ash billowing at the margins of the column, the moving mean of the signal was calculated over a time window of 300 s, the smallest for which climactic phases resulted in a steady signal. Conceptually, the average Apparent Temperature ( $AT_{av}$ ) gives information on the density of 'hot' pixels within the AOI; a sudden increase corresponds to an impulsive increase in erupting masses captured in the area; steady  $AT_{av}$  corresponds to non-eruptive conditions or steady eruptive phases.

## 2.3 Radar data analyses

A weather radar is a mono-static system that consists of a transmitter and one receiver, equipped on a real aperture antenna, through which it sends a sequence of impulse signals and receives their echo. This system is specifically designed to detect clouds and precipitation particles, measuring backscattered signal named radar reflectivity factor, to the radar by detected particles/clouds. It uses the signal's amplitude, phase, and polarization of the scattered electromagnetic wave, to infer relevant properties of particles [Montopoli et al. 2023]. The scanned volume is sampled along 12 elevation angles for each azimuthal angle and for each range bin. Then the data of whole probed volume is released every 10 min (radar operative time sampling [Marzano et al. 2020]). Elaborating on the measured copolar radar reflectivity  $Z_{hh}$  (dBZ) and applying the consolidate Volcanic Ash Radar Retrieval (VARR) methodology, we extracted the primary quantitative information about volcanic clouds [Marzano et al. 2020; Mereu et al. 2023; 2024]. This algorithm consists of two sequential steps after the detection: 1) the maximum a posteriori (MAP) classification of tephra classes, and 2) the estimation of tephra concentration  $C_t$  ( $\text{g m}^{-3}$ ) and mean diameter  $D_n$  (mm) in each detected range-bin volume, using the forward analytical model. The latter generates physically-based random tephra classes, utilizing available microphysical and statistical characteristics from the literature [Mereu et al. 2023; 2024]. We estimated the top plume height  $H_{TP}$  (km) above the summit craters (approximately 3350 m a.s.l.) using a threshold algorithm applied

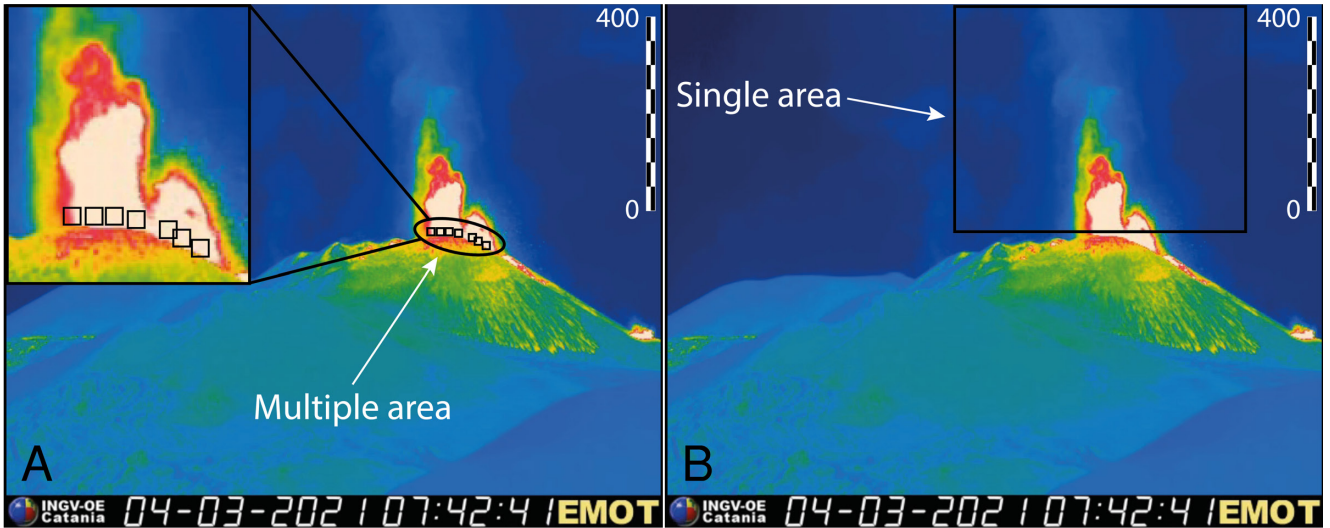


Figure 4: Example of areas used during Multiple area (MA) and Single area (SA) analyses. [A] Multiple Area, with the 100 px<sup>2</sup> areas positioned above the SEC active vents; [B] Single Area, with a single area above the SEC (Time is expressed in UTC; Scale bar computed at the crater, adjusted for camera distance and viewing angle).

to the measured  $Z_{hh}$  of the probed volcanic plume, with an uncertainty of  $\pm 300$  m with respect to the axis of the beam cone, due to scanning radar geometry. Given the time-space variation of  $C_t$  and applying the continuity equation to  $C_t$ , defined as the Mass Continuity Approach (MCA) [e.g. Mereu et al. 2015; Marzano et al. 2020], we quantified the time variation of mass  $M_t$  (kg) for the discretized time-space domain of the radar geometry [Mereu et al. 2023; 2024]. At each radar detection, we evaluated the Mass Eruption Rate (MER; kg s<sup>-1</sup>) given by:

$$\begin{aligned} \text{MER} &= \text{MER}_{\text{diff}} + \text{MER}_{\text{adv}} \\ &= \frac{\partial M_t(t)}{\partial t} + \oint_S C_t(\mathbf{r}, t) [\hat{\mathbf{n}}_s(\mathbf{r}, t) \cdot \mathbf{v}(\mathbf{r}, t)] dS, \end{aligned} \quad (1)$$

where  $\text{MER}_{\text{diff}}$  and  $\text{MER}_{\text{adv}}$  are the derivative mass rate and the advection mass rate, respectively. The  $\text{MER}_{\text{diff}}$  allowed evaluating the time-space variation of the tephra mass  $M_t$  enclosed within each radar volume including the closed plume surface  $S$  detected by the weather radar scan.  $\text{MER}_{\text{adv}}$  accounts for the tephra mass transported outward across the surface of each radar bin by the horizontal velocity, where  $\mathbf{r}$  is the range vector,  $\mathbf{n}$  is the unit vector normal to the surface  $S$ , and  $\mathbf{v}$  is the tephra velocity field.

The MER retrieval depends on the intensity of the explosive event, the maximum plume height ( $H_{\text{TP}}$ ) and the radar sampling time [Mereu et al. 2015]. As tested in Marzano et al. [2020] and Mereu et al. [2022, 2023], the MER retrievals for Etna explosive events ranged from  $10^2$  to  $10^7$  kg s<sup>-1</sup>, whereas the  $H_{\text{TP}}$  estimates ranged from 1 to 12 km above the vent. Radar data reveal the ash mass balance in the eruptive column above the eruptive vent; they are however able to detect only MER oscillations occurring at timescales comparable or larger than the radar sampling time.

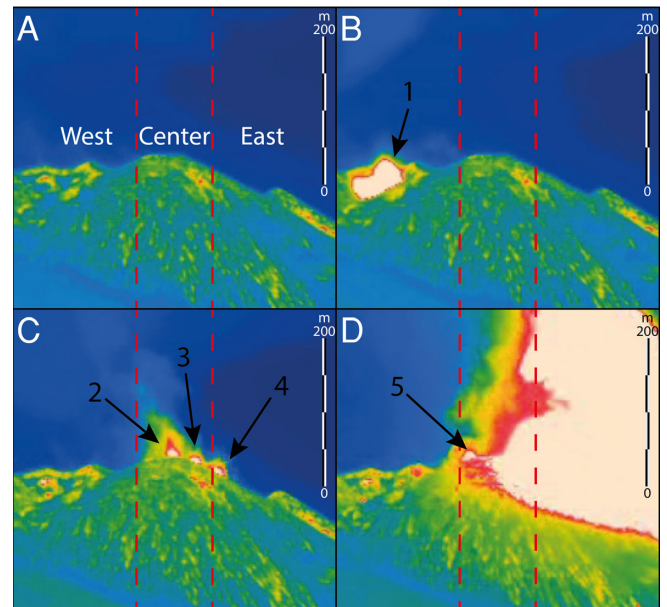


Figure 5: Zoom on the SEC cone from the EMOT camera frames. [A] shows the sectorization of the SEC cone. [B]–[D] show multiple vents that activate during the 28/02/2021 eruption (P3). During the beginning of the climactic phase, focused on the eastern sector, [D] the centre-western sector is still showing a pulsatory activity. Scale bar computed at the crater, adjusted for camera distance and viewing angle.

### 3 RESULTS

#### 3.1 Visual observations of thermal videos: eruption dynamics

All of the studied eruptions included precursory activity that consisted of low intensity Strombolian explosions that generated small clouds of relatively cold (to thermal camera sensor perspective) gas and ash that rose from a few tens up to a hun-

dred of meters above the crater rim. This precursory activity involved different portions of the crater (Figure 5A). Multi-vent activity was common in all studied eruptions (Figure 5B–5D). Typically, 3 to 7 vents (sometimes also about 15 m from one another) were observed in which pre-fountaining, Strombolian activity was concentrated. The number of active vents increased with time until the paroxysm, when they became indistinguishable. Vent activation could start from any crater sector and progress laterally in all sectors (Figure 5). There were at least two active sectors in each eruption. Vents from the central sector, either activated at the beginning or just before the onset of the climactic phase, were usually involved in the eruption, while eastern and western sectors were sometimes “inactive” except for sporadic ash emissions. Typically, activation of vents from a new sector was associated with a decrease in intensity of explosions in the others (Supplementary Material Figure S2a, S4a, S5a, S6a, S7a). For example, in P7, the activity took place mainly in the western sector (vents from a to e; Figure 6A and 6D). However, at the end of the eruption a vent in the eastern sector (f in Figure 6A and 6D) became active when the activity of the vents in the western sector decreased. Multiple vents located in the western sector typically produced separated jets inclined to the SW whose bursts are still visible during the climax of lava fountaining.

Based on video observations and eruptive behaviour across all studied events, we define four-phases of the typical sequence of paroxysmal activity at SEC, described below.

### 3.1.1 Strombolian phase

In the early stages, the eruptive intensity is mild (1 to 3 explosions every 5 minutes); eruptive material is ejected up to a few metres over the crater rim, and the aura of the explosion can be barely detected in thermal images and by small spikes in the  $AT_{av}$  signal. The activity within the crater increases in both intensity and frequency with time: at explosion frequencies of about 1 per minute, the jet can reach about 50 m above the crater rim and at 4–6 explosions per minute the jet rises from 80 to 120 m above the crater rim. Long lasting (i.e. 8 hours) precursory activity can be steady for prolonged periods (e.g. P5 eruption); short lived fountaining episode does not have long precursory phase (e.g. P3 eruption). In some eruptions, as during the February–April 2021 eruptive crisis, persistent Strombolian activity could occur between paroxysms for hours/days (e.g. P2 eruption).

### 3.1.2 Waxing phase

The duration of this phase can range from 7 to 35 minutes (Table 2), during which the increase in intensity and frequency of Strombolian activity eventually results in mild fountaining (as reported also in Calvari et al. [2021]). Individual bursts from single vents become indistinguishable as explosions form a single large jet. The activity therefore results in a pulsatory behaviour with almost continuous ejection of incandescent material. At this time the ejecta reach heights ranging from 150 to 200 m. As the activity goes on, the jet height gradually increases up to 450–550 m above the crater rim, eventually forming an ash-charged turbulent plume. In some cases, the jet height can reach up to 1000 m in the minutes preceding

the climactic phase. The number of active vents increases. (Figure 6).

### 3.1.3 Climactic phase

The climactic phases are characterized by an approximately stable fountain jet height (that differs from each episode) and a less pronounced pulsatory behavior. This phase is marked by a continuous emission of incandescent material, with the jet width reaching a scale comparable to the crater. Durations of these phases ranged from 30 minutes to 2 and a half hours. In the climactic phases, the eruption columns rise up to 9 km above the vent, as estimated by the radar and listed in Table 3. The outer portion of the columns can be also marked by turbulent interaction with the surrounding atmosphere generating cold ash billowing that may hinder partially or totally the jet (e.g. P1, P3 eruptions).

### 3.1.4 Waning phase

Lava fountain height starts to decrease significantly during this phase. Pulsatory behaviour becomes pronounced again, resulting in mild fountaining that becomes progressively less energetic. Eruptions in our dataset end abruptly; within 5 to 15 min the jet drops down to a few hundred meters above the crater rim and then switches into oscillatory and discontinuous, ash-poor jets, typical of Strombolian activity. Within 3 to 64 min the activity reduces to a single vent or is completely shut down.

## 3.2 Thermal analysis

Based on the signal pattern derived from MA and SA, we defined four trends that are corresponding to the specific eruptive phases (Section 3.1) and a background level that varied among the eruptions analysed because of variable atmospheric conditions (and probably characterized by a mild activity that cannot reach the crater rim). The thermal-signal response throughout the four phases can be described as follows: in the “Strombolian phase” the signal is marked by individual spikes rising from background values, corresponding to minimal vent activation and bursts that barely extend beyond the crater rim; in the “Waxing phase” the  $AT_{av}$  is increasing but still marked by significant spikes, meaning a steady increase in both mass and height of the activity, resulting in an ever-larger occupation of the AOI, with occasional major bursts being observed; In the “Climactic phase”  $AT_{av}$  oscillates about its maximum and can form a plateau (Figure 6). Absolute values may differ for each eruption, depending on the proportion of the AOI covered by saturated pixels. Even when AOI are not fully saturated (e.g. the eruption affects only a crater sector),  $AT_{av}$  remains stable around the event’s highest values during this phase. The lava fountain is fully developed; the “Waning phase” is marked by a signal decrease, still punctuated by significant spikes. The lava fountain jet tends to lower with time (sometimes abruptly), decreasing the number of saturated pixels in the AOI. The zone where the AOI are located continues to be influenced by the heat of the emitted gas. Strombolian explosions of variable intensity can take place during this phase. The  $AT_{av}$  clearly documents asynchronous activation of each vent area in every eruption (Figure 6A), with no sys-

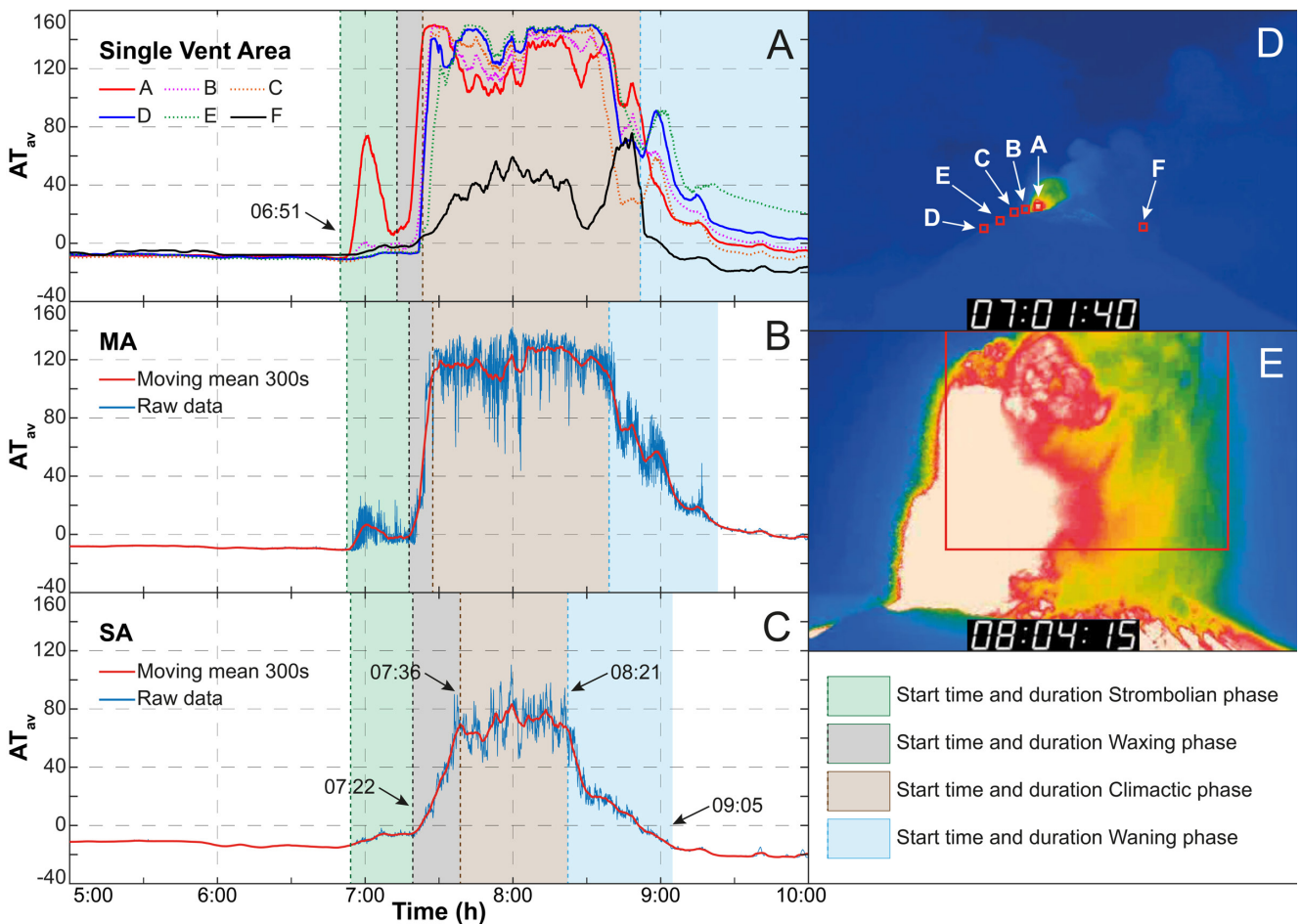


Figure 6: Eruption P7: comparison between [A] Single vent area, [B] Multiple area, and [C] Single area signals. [D] and [E] thermal snapshot from the EMOT camera frames showing the location of vents active during this eruption and the related areas analysed for the single vent area and multiple area methods during the pulsatory phase [D], and single vent area of analysis during the climactic phase [E]. Time is expressed in UTC.

tematic pattern relative to their position and number. The total time required for the activation of all vents ranges from 2 to 303 min. Generally, the closer the vents, the shorter the time gap between their activation. Temperature at the different vents can also change in parallel or be anticorrelated.

The climactic phase is defined by the saturation of most vent signals. MA signal better describes the general eruption dynamics, rising from the background during the initial Strombolian activity, culminating in a plateau during the steady fountaining phase, and decreasing rapidly to background values when the fountain winds down (Figure 6B). The SA signal can efficiently describe the eruption dynamics, with a similar pattern with respect to MA (Figure 6C). It can also record the Strombolian phase and closure of the eruption, but it is less sensitive to small intensity Strombolian burst with respect to the MA. SA is also more sensitive to the weather conditions as it analyses a greater area of the atmosphere above the craters, which could be occupied by storm clouds or mist.

As an example, Figure 6 shows the variations of all the studied parameters (moving mean 300 s of single vents 6 a, MA 6 b, SA 6 c) for the eruption P7, a type example of eruptive dy-

namics within the analysed dataset. In the hours preceding the fountain, all the parameters remained approximately constant at background values. In parallel, SA decreases towards lower background levels at around 06:00 (Figure 6C). These oscillating background values were related to the presence of meteorological clouds, until the sky cleared around 06:00, uncovering a greater portion of the AOI determining lower  $AT_{av}$  values. At 06:51 only one vent was active (Vent A in Figure 6A); within 39 minutes, four further vents started emitting magma (Strombolian and Waxing phase). The parameters started rising from the background at around 06:53 (MA) and 06:55 (SA) (Figure 6B, 6C) peaking at 07:04 (MA) and 07:06 (SA) and then decreased almost to background levels (associated with the temporary shutdown of vents A and B). At 07:20 the signals rapidly increased (Waxing phase) to saturation values (8 min MA; 14 min SA) and from 07:28–8:33 (MA) and 07:36–08:21 (SA) remained steady (Climactic phase).  $AT_{av}$  decreases to background level in about 51 min (MA, Waning phase) while the sky is clear already at 09:05 (SA, closure of the eruption).

Calculated time evolution of all the studied eruptions is shown in Table 2. The climactic phases range from 10 to 40% of the total eruption duration, which ranges from 10 to

Table 2: Based on MA (for the Strombolian Phases) and SA (for the timing of Waxing, Climactic and Waning phases)  $AT_{av}$  signal we assign duration of these phases in each studied fountain. Time is expressed in UTC.

N°	Active vents	Start–end (duration, minutes)				Remarks
		Strombolian phase	Waxing phase	Climactic phase	Waning phase	
P1	3	14:05–16:02 (117)	16:02–16:32 (30)	16:32–16:44 (12)	16:44–17:09 (25)	Wind towards S–SE partially hiding Strombolian phase and Waning phase.
P2	7	07:52–08:47 (55)	08:47–8:59 (12)	08:59–09:45 (46)	09:45–10:05 (20)	-
P3	5	07:17–07:45 (28)	07:45–08:05 (20)	08:05–08:32 (27)	08:32–08:35 (3)	This eruption ends abruptly. After that $AT_{av}$ values record the heat above the crater.
P4	7	00:20–07:45 (445)	07:45–08:20 (35)	08:20–09:24 (64)	09:24–09:39 (15)	-
P5	7	01:27–06:09 (289)	06:09–06:25 (16)	06:25–06:54 (30)	06:54–07:16 (22)	1 lava fountaining attempt between 04:16 and 05:22.
P6	4	09:05–09:55 (50)	09:55–10:02 (7)	10:02–10:12 (10)	10:12–10:26 (14)	Mild and short-lasting fountaining activity from the W sector.
P7	6	06:51–07:22 (31)	07:22–07:36 (14)	07:36–08:21 (45)	08:21–09:05 (44)	-

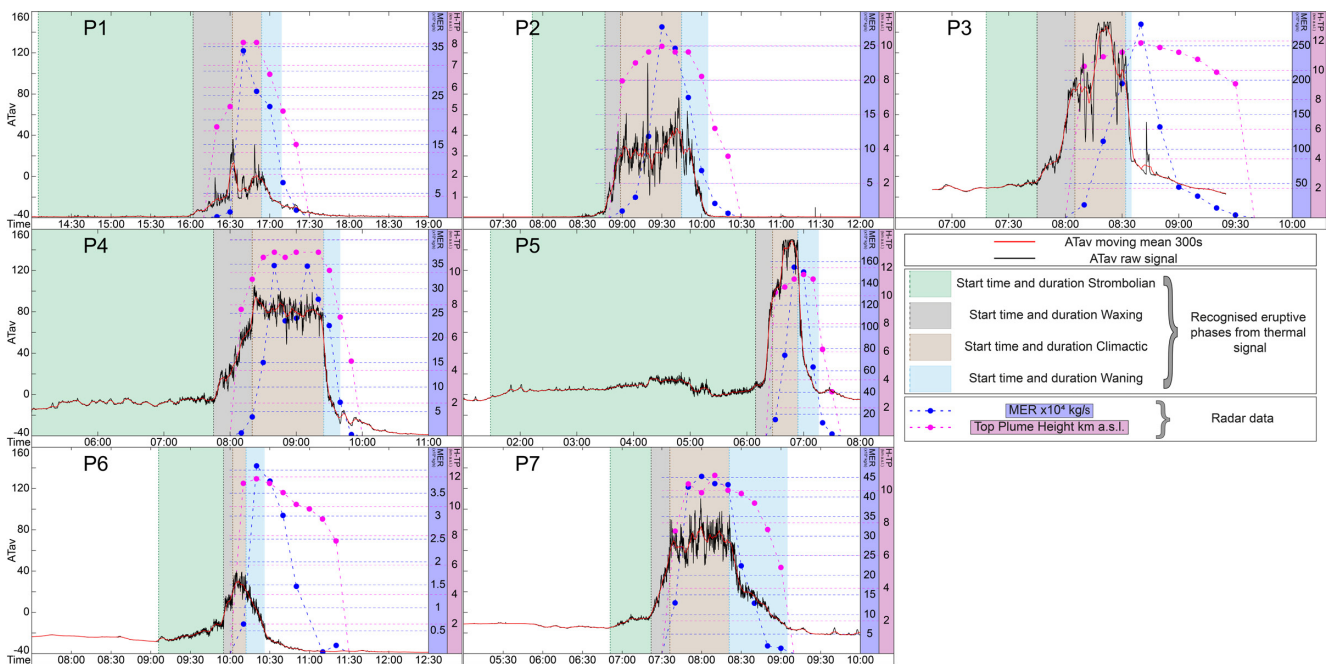


Figure 7: Comparison between the SA thermal signal and the radar data related to the column height ( $H_{TP}$ ) and MER.  $AT_{av}$  scale is maintained constant; time series,  $H_{TP}$  and MER data varies based on intensity and duration of each eruption. Time is expressed in UTC.

64 min. The Strombolian phases last from 25 to 80% of the eruption, ranging from 28 to 445 min. Transitions between phases were identified using both MA and SA methods. We

used both approaches because they are complementary: MA, which averages measurements from small areas, is more sensitive to small Strombolian bursts but typically saturates dur-

Table 3: Table showing a summary of Radar data and the maximum jet height derived from processing thermal-infrared camera (ENT) frames as described in [Mereu et al. \[2020\]](#).

N°	Eruptive phase	Max $H$ jet ( $\pm 5$ m a.v.)	$H$ Top-plume (km a.s.l.)	Estimated MER ( $\times 10^4$ kg s $^{-1}$ )	Additional remarks
P1	Strombolian	650	0	0	Plume remained 20 min after the end of waning phase between 4.9 and 3.37 km (MER 7.21–1.4). Max $H$ jet affected by the ash plume covering.
	Waxing	265	4.17–5.11	0.19–1.17	
	Climactic	150	8.06	34.13–25.85	
P2	Waning	200	6.6–4.9	22.7–7.21	Plume remained 20 min after the end of waning phase between 5.18 and 3.57 km (MER 2.09–0.66).
	Strombolian	300	0	0	
	Waxing	430	0	0	
P3	Climactic	930	7.95–9.96	0.98–27.77	$H_{TP}$ and MER peaked after the end of waning phase, because of the strong wind (50–75 km h $^{-1}$ between 9 to 13 km a.s.l.). Plume remained $\approx 70$ min after the end of
	Waning	480	9.64–8.22	17.49–6.88	
	Strombolian	350	0	0	
P4	Waxing	830	0	0	Plume remained 20 min after the end of waning phase between 7.25 and 4.57 km (MER 6.87–0.3).
	Climactic	4135	0–11.23	0–195.01	
	Waning	3785	$\approx 11.23$	$\approx 195.01$	
P5	Strombolian	780	0	0	Plume remained $\approx 20$ min after the end of waning phase between 6.19 and 3.3 km (MER 12.08–1.71). Max $H$ jet affected by the cloud covering.
	Waxing	2375	0–9.57	0–3.87	
	Climactic	4165	10.91–11.23	14.98–34.72	
P6	Waning	2255	10.12–7.25	22.49–6.87	Plume remained $\approx 65$ min after the end of waning phase between 11.55 and 7.64 km (MER 3.75–0.17).
	Strombolian	480	0	0	
	Waxing	-	0	0	
P7	Climactic	-	10.28–11.23	15.01–154.98	
	Waning	-	11.55–11.22	150.46–63.41	
	Strombolian	590	0	0	
P6	Waxing	890	0	0	
	Climactic	830	0–11.55	0–0.64	
	Waning	300	11.87	4.09	
P7	Strombolian	650	0	0	
	Waxing	1975	0	0	
	Climactic	3235	7.5–10.9	13–45.26	
P7	Waning	2770	9.8–5.2	22.41–1.38	

ing the Waxing phase; SA, by contrast, better captured the rising trend of the Waxing phase and the nearly stable behaviour of the Climactic phase. Furthermore, the discrepancy with the start and end times of the eruptions reported in [Table 1](#) estimated by [Calvari and Nunnari \[2022\]](#) is primarily due to differences in the methodologies used. Specifically, we assigned phase start- and end-times based on changes in our signal. As such, these timings can be considered as objectively reflecting the actual state of the eruption (i.e., what actually happened at the eruptive vent).

It should be noted that the estimates of  $H$  of the lava fountain jet ([Table 3](#)), obtained by processing the frames from the ENT camera, show that among all the analysed eruptions the maximum  $H$  jet occurs during the climactic phase, but for the cases P1 the maximum  $H$  jet occurs during the Strombolian phase. This difference could be due to the volcanic plume that during the climactic phase was directed toward the south direction, partially covering the lava fountain jet.

### 3.3 Radar data

MER and  $H_{TP}$  estimates derived by processing the radar measurements for the seven Etna eruptions analysed are summarized in [Table 3](#). In the Strombolian and Waxing phases,

radar measurements typically do not allow for the calculation of  $H_{TP}$  and MER because the eruptive cloud consists mainly of gas and fine ash particles that are not precisely detected by the radar. The exception are P1 and P4, where retrieval was likely enhanced by favourable atmospheric conditions [[Mereu et al. 2023](#)].

In the climatic phases the  $H_{TP}$  ranges between 8 and about 12 km a.s.l., whereas the MER shows values ranging among  $10^4$  kg s $^{-1}$  (P6),  $10^5$  kg s $^{-1}$  (P1, P2, P4, and P7), and  $10^6$  kg s $^{-1}$  (P3 and P5). In the waning phase,  $H_{TP}$  and MER usually decreased proportionally with the intensity of explosive activity, but in some cases (P3 and P6), they exhibited nearly constant or slightly increasing trends before gradually declining.

In [Figure 7](#), the MER and plume height ( $H_{TP}$ ) peaks calculated from RADAR data (blue and magenta dashed lines respectively) are shifted forward up to 20–30 minutes with respect to the climactic phase as detected from thermal observation at the vent, because of the delay in between ejection of the pyroclastic mixture and the radar acquisition times. Plume height ( $H_{TP}$ ) peaks are also sustained for longer times with respect to the temperature peaks measured by the thermal camera because of advection diffusion effects associated with high level atmospheric winds.

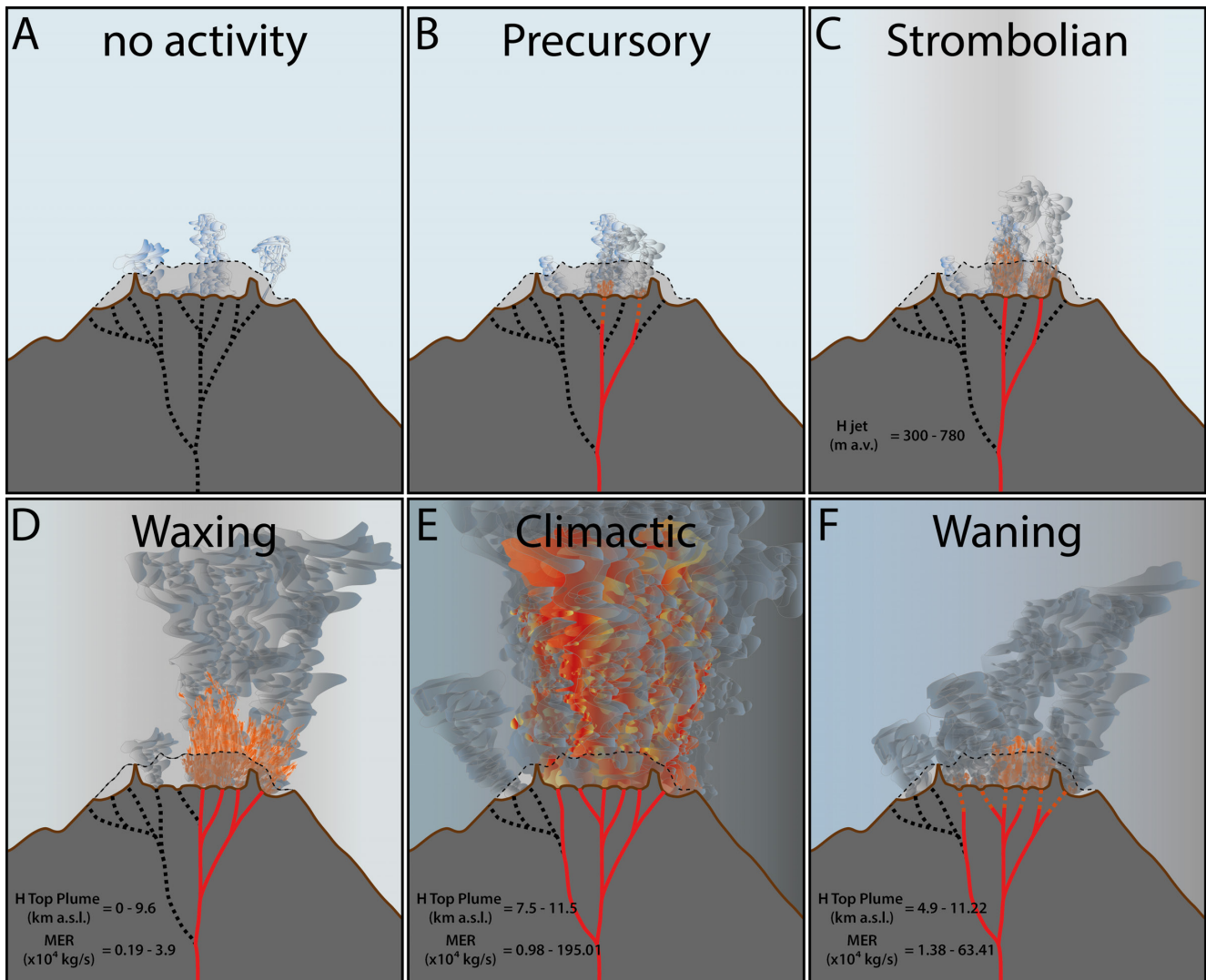


Figure 8: A conceptual model of the evolution of the Etna lava fountains at SEC. [A] “no activity” characterized by passive degassing; [B] Precursory phase with more intense degassing driven by ascending magma. Reopening of pre-existing fractures and mild Strombolian eruptions occur; [C] Full opening of previously activated fractures, with more frequent and more intense Strombolian eruptions; [D] Opening of additional pre-existing fractures. Activity increases in intensity and frequency, producing mild lava fountaining; [E] New conduits may still open at the beginning of this phase. The climactic phase is characterized by the establishment of an approximately stable eruption column. Plumes reach their maximum height and MER; [F] Eruptive activity decreases in intensity and frequency, returning first to mild fountaining and then to progressively weaker Strombolian activity. In this phase activity is no longer fed and the magma level in the conduit drops down.

## 4 DISCUSSION

### 4.1 Validity of the $AT_{av}$ parameter

The study of the thermal signals can be a fundamental tool for deepening our knowledge of eruptive behaviour and constraining the transition between different styles of eruptive activity as objectively as possible.  $AT_{av}$  parameter is linked to the apparent temperatures recorded by the thermal camera and can be used to document the eruptions and place a solid constraint on the transition between Strombolian activity and lava fountaining. Its calculation can be done in real time, as it requires few computational resources from radiometric RGB images routinely saved in monitoring activities.

Among the parameters analysed in this study, SA is the most efficient as it does not require setting vent locations (which varied among eruptions and are thus difficult to forecast) and best depicts variations in eruption intensity. The use of the same wide area positioned upon the SEC allowed collection of representative data for all the eruption dataset. It could also efficiently detect the Strombolian phase (Figure 6C). The MA signal is able to describe the eruption dynamics but can be used only for analyses *a posteriori* because it requires the identification of active vents (Figure 6B).

This parameter records eruptive transitions as a gradual and continuous process given by increasing both frequency and energy of the pulses until the continuous lava emission is achieved. Climactic phases are recorded as plateaus with only

minor fluctuations. During the climatic phase, the plateau can be attributed to the density of saturated pixels that remains nearly constant within the AOI. The differing heights reached by the fountains after each pulse, which alternately vary the density of saturated pixels in the AOI (e.g. low–high–low), could enable identification of the pulses within the lava fountain dynamics.

The potential of the  $AT_{av}$  parameter for the detection of paroxysmal phases is not just due to its ability in discriminating between low and high intensity activity, but it is also relevant for the clear identification of the transitions between them. The identification of the transitional phase is a critical step for the setup of a procedure of an early warning system for lava fountains occurring at summit cones. This could be possible after the study of a larger eruptive dataset covering the full variability spectrum of the transitional dynamics in paroxysmal eruptions.

## 4.2 Dynamics of paroxysmal activity

Observations from the seven studied eruptions reveal a consistent eruptive pattern characterized by a progression from low-intensity Strombolian explosions to high-energy lava fountaining, followed by a rapid decline in activity. This sequence involves a complex spatial and temporal evolution of vent activity, reflecting dynamic interactions between gas accumulation, magma flux, and conduit conditions.

The precursory activity probably heralding the rise of the magma level, is mainly dominated either by intermittent gas emission ('puffing' sensu Harris and Ripepe [2007], Patrick et al. [2007], Leduc et al. [2015], and Gaudin et al. [2017a,b]), ash venting or weak Strombolian explosions (about one every 5 minutes at each vent, ejecting material up to the crater rim or below it) that persisted for hours. A progressive increase in the intensity of the activity leads to more energetic, more frequent Strombolian explosions. In parallel, new vents open within the crater (Figure 8), at variable distances from the active one. Their arrangement and timing of activation suggest the progressive opening/reopening of a network of shallow fractures with a direction approximately W-SW/E-NE connected with a deeper reservoir.

One of the most distinctive features observed in this study is the asynchronous activation and alternation of vents within the SEC crater. This alternating activity between central/eastern and western vents may indicate a lack of shallow-conduit connectivity within these two sectors and a possible connection to a deeper reservoir beneath the SEC cone base. In this scenario, new vent opening or intensified explosive emission rate at one sector may induce a transient pressure drop and lower the free magma surface in the already active conduit [Bonaccorso et al. 2004].

The multiplicity of vents that become active, their spatial distribution, and the timing of their activation suggest the presence of a complex shallow fracture system within the SEC. Given the inherently fragile nature of scoria cones such as the SEC, the arrangement of vents and the dynamics of these shallow conduits are important features to monitor. Indeed, the existence of numerous conduits within already fragile cone structures may promote flank instability of the cone, leading

to cone collapses and the generation of pyroclastic density currents (such as those that occurred on 10/02/2022 [Zuccarello et al. 2025] and on 02/06/2025—INGV-OE reports\*).

Transitional activity between sectors implies the formation of a pulsatory jet almost as large as the crater; and rapidly (7–50 min) leading to the climactic phase of fountaining activity, which generates several km high columns and ash charged plumes [Alparone et al. 2003]. This style of activity and eruptive sequence has been observed and described at other mafic volcanoes, such as Villarrica [Romero et al. 2018] and Kīlauea [Walker et al. 2023]. The phases described in the latter study, in particular, closely mirror those we observed for the Etna eruptions analysed here. As reported, the 2018 lower East Rift Zone fissures at Kīlauea were preceded by Strombolian activity [Houghton et al. 2021; Walker et al. 2023]. Over time, the increasing intensity and pulse frequency make individual explosions indiscernible from one another. The onset of this pulsatory behaviour—termed “unsteady Hawaiian fountain”—corresponds to the waxing phase in our eruption dataset. In both cases, this phase is characterised by multiple, closely spaced, and overlapping pulses. Finally, when the pulses become so closely spaced that they produce an almost continuous jet of material, the climactic phase occurs; this is referred to as a “steady Hawaiian fountain”. During this phase, pulse fluctuations are minimal or very brief, and a stable ash column typically forms. At the end of this phase, fountaining activity ceases abruptly, and Strombolian explosions resume (as noticed also at Villarrica by Romero et al. [2018]); their intensity rapidly decreases until the complete cessation of the eruptive event, although the ash plume can persist for more than an hour.

## 4.3 Thermal and radar monitoring comparison

Thermal and radar data show generally good agreement in tracking eruption intensity (Figure 7), though differences arise due to the sensor resolution and plume behaviour. The waxing phase and the initial part of the climactic phase of the eruption are recorded by the increase of the height of the eruptive column ( $H_{TP}$ ), while the MER increases more slowly in these phases, accounting for the limitation imposed by time sampling of the radar. The radar signal detects pyroclastic material in the atmosphere about halfway through the waxing phase in events P1, P2, and P4, while in the other cases directly in the climactic phase. In the climactic phase, the greatest increase of the MER is recorded. The  $H_{TP}$  signal increases significantly in the waxing phase and the beginning of the climactic phase (51.8 to 85.2% of the total height). Within the climactic phase, minor variations (on average from 11–20%, and some cases up to 36%) were calculated.

Both thermal and radar signals peak in the  $AT_{av}$  climatic phase, except for P3 and P6 eruptions. In P3 the wind speed (61–81 km h<sup>-1</sup> between 10 and 12 km a.s.l.) and direction (North/West to South/East) could influence the measurement. In P6, the duration of the fountain was very short (17 minutes including both waxing and climactic phases), not steady, and had no significant waxing phase; the  $H_{TP}$  peaked when the eruptive column was not fed anymore. This mismatch could

\*Available at [www.ct.ingv.it](http://www.ct.ingv.it)

be due to the combination of the short duration of the activity and the radar scanning and pre-processing time. We highlight that all radar measurements and the related estimates, including MER, consider both the time required for probing the entire volume and the time necessary for pre-processing the raw data (about 10 minutes). Similar mismatching can be found combining radar retrievals with infrasound records, where the maximum height of volcanic plume is typically detected by the radar after the short climactic phase [De Angelis et al. 2023].

The waning phase is well represented by the MER signal, which decreases almost simultaneously with the  $AT_{av}$  signal. On the other hand, the radar detects an active plume up to an hour after the end of the waning phase, indicating the presence of pyroclastic materials in the atmosphere (specifically in the region above the SEC scanned by the radar) even after the column is not fed anymore. It is worth noting that the  $H_{TP}$  is not necessarily correlated with the MER, as MER estimation is affected by atmospheric conditions and mostly reflects the plume ash content.

#### 4.3.1 A model for Etna's feeding system

We propose a model for the structure of feeding system during a paroxysmal eruption. The observed dynamics are consistent with the involvement of a magma batch of finite volume [Murru et al. 1999; Chiarabba et al. 2000; Patanè et al. 2002; 2003; Métrich et al. 2004; Spilliaert et al. 2006a; b; Corsaro et al. 2007; Puglisi et al. 2008; Collins et al. 2009; Ferlito and Lanzafame 2010; Corsaro et al. 2013]. Mt. Etna is characterized by a multi-level magma storage system [Bonforte et al. 2008; Kahl et al. 2015; Calvari et al. 2020; De Gori et al. 2021; Palano et al. 2024]. The first, a larger and deeper reservoir lies at mid-crustal depths (approximately 6–8 km below sea level), is the source of the most primitive magmas erupted during large paroxysms or flank eruptions [Corsaro et al. 2009; Cannata et al. 2018]. A second shallower reservoir is located near sea level and is associated with the small-scale paroxysmal activity. Some authors have also proposed the presence of an additional small reservoir within the volcanic edifice, directly beneath the South-East Crater (SEC) at roughly 1 km depth below the vent [Behncke et al. 2006; Bonaccorso et al. 2011; 2013]. This reservoir contains relatively crystal rich and gas poor magma, [Kahl et al. 2011; 2015; Giuffrida and Viccaro 2017].

The entire plumbing system appears to be pressurized, with the shallowest 1 km deep reservoir being partially isolated or not efficiently connected to the main conduit (always filled with magma) that links the sea-level reservoir to the more superficial storage region [De Gori et al. 2021; Paonita et al. 2021]. When new magma input from the sea-level reservoir occurs, overpressure develops within this connecting conduit, either by mechanical injection of new magma or accumulation of a gas phase that cannot be efficiently released through pre-existing fractures [Caricchi et al. 2024; Palano et al. 2024]. When the overpressure stress overcomes the tensile strength of the host rocks, new fractures form and permeability of the system increases. This leads to an increase in gas flux into the shallow storage that can raise magma level and trigger

the Strombolian phase [Allard 2010; Paonita et al. 2021]. If the permeability of the system allows equilibrium outgassing, prolonged Strombolian activity can be sustained without any significant increase in explosivity [Farquharson et al. 2016; Crozier et al. 2022]. If equilibrium outgassing does not occur, the overpressure keeps building up until the opening of new fractures or reactivation of pathways for magma and gas migration. A relatively rapid pressure drop, caused by the opening or widening of fractures, enhances volatile exsolution from the magma [Ripepe et al. 2005; Spampinato et al. 2015]. As a consequence, the rate and intensity of explosions increase and lead to the onset of the Waxing phase. In parallel, increase of pressure allows the opening/reopening of fractures that are either connected with the shallow reservoir or form as secondary branches of the main conduit. Once a critical combination of pressure and volatile content is reached, the conduits can be considered efficiently connected with the shallow reservoir. At this stage the gas and magma flux typically becomes continuous, marking the Climactic phase of the eruption (e.g. sustained fountaining). The end of the eruption is marked by a decrease in all monitoring signals (multiparametric studies on Etna show concurrent declines in all geophysical data [Calvari and Nunnari 2022]). Strain measurements indicate a deflation of the entire edifice [Bonaccorso et al. 2013; Aloisi et al. 2018; Currenti and Bonaccorso 2019].

According to our conceptual model, Etna's eruptions dynamics are primarily governed by the volatile content of the magma. Volatiles are released during the compression-decompression phases in the conduit due to the rise of new fresh magma. An increase in overpressure within the conduit promotes the opening or widening of fractures. The consequent pressure decrease in the conduit enhances volatile exsolution and thus increases the bubble content. In this phase volatiles are released into the surface reservoir from which Strombolian eruptions are generated. Finally, when the conduit becomes efficiently connected to the shallow reservoir, bubbles may become effectively coupled to the magma column and a sustained bubble–melt flux [Walker et al. 2023] is established, producing the climactic phase of the eruption.

## 5 CONCLUSIONS

Based on eruption observations, the analyses of  $AT_{av}$  thermal signal, and its comparison with radar data, we can conclude that there is no threshold behaviour that marks the transition from Strombolian activity to lava fountain; transition occurs through continuous increase in intensity, frequency of explosions and height of the emissions from separate vents, until merging into a single, almost continuous jet, which we associate to the onset of the fountain and to the climactic phase of the eruption. This increase can be slow (28–35 minutes) or fast (7–15 minutes) regardless of the average intensity of the eruption in our analysed dataset.

Four phases have been recognised during Etna lava fountain episodes:

- A Strombolian phase, initiated by the rise of a gas phase (arrival of primitive magma), in the superficial reservoir hosting crystal rich, degassed magma.

- A Waxing phase, eventually leading to mild fountaining activity. During this phase, because of the overpressure in the main conduit, new fractures are opening or existing ones are widening, resulting in multiple vent activation.
- A Climactic phase, in which the gas and magma emission is continuous, resulting in an almost stable lava fountaining. Fountaining requires full connection between the main conduit and the reservoir feeding Strombolian activity.
- A Waning phase, in which the activity decreases down to a sequence of Strombolian bursts. This phase is associated with the deflation of volcanic edifice and a mechanical re-coupling of fractures.

The presence of multi vent activity, the spatial distribution of vents and their timing of activation reflect the presence of a complex network of shallow conduits within the SEC cone. This already existent network together with the opening of new magma ascent pathways could increase the instability of the SEC, eventually leading to cone collapses and pyroclastic flows. Averaging data from selected AOI in RGB colour coded thermal images allows for fast and efficient eruption monitoring. A single large area of interest (SA method) has proven to be the most efficient as a real time monitoring signal, since it provides a description of the ongoing eruptive activity and does not require operator intervention. Monitoring areas above single active vents allows detailed analyses of the eruptive activity (sectors involved, activation times and dynamics of the conduit), but they require manual positioning of the AOI and can therefore be fully exploited only during a *posteriori* analysis.

Comparison of thermal and radar data allow determination of the relationships between vent activity and plume formation, confirming the use of radar as a fundamental tool for early warning and first-stage characterization of eruptive events. At the same time, the strong correlation of MER retrievals with the  $AT_{av}$  is, in most cases, particularly promising. It confirms that simple frame processing of low-cost sensors, such as thermal cameras, is highly effective for detecting volcanic eruptions and for identifying distinct eruptive phases. Finally, we remark that the main limitation of these methods is their inability to retrieve good quality data when meteorological conditions are poor; and that the fountain jet can be also partially to totally covered by ash billowing from small crater rim collapses, or fallout from the eruptive cloud.

## AUTHOR CONTRIBUTIONS

Francesco Amadio: Writing – original draft, Visualization, Validation, Investigation, Formal analysis, Data curation, Conceptualization. Laura Pioli: Writing – review & editing, Supervision, Project administration, Funding acquisition, Formal analysis, Data curation, Conceptualization. Simona Scollo: Writing – review & editing, Supervision, Project administration, Funding acquisition, Formal analysis, Data curation, Conceptualization. Vignoli Giulio: Formal analysis. Luigi Mereu: Writing – review & editing, Formal analysis, Data curation. Emilio Pecora: Writing – review & editing, Instrument curation, Data curation.

## ACKNOWLEDGEMENTS

This publication was produced during F.A. PhD course, XXXVIII cycle, in “Scienze e Tecnologie della Terra e dell’Ambiente” at the University of Cagliari, with the support of a scholarship funded by Ministerial Decree No. 351 of 9.4.2022, under the PNRR—funded by the European Union—NextGenerationEU. The work was partially supported by the project F73C23001610007 funded by Fondazione di Sardegna (to L.P.). This research was also performed in the framework of the INGV Project “Pianeta Dinamico” (D53J19000170001), funded by MUR (“Ministero dell’Università e della Ricerca, Fondo finalizzato al rilancio degli investimenti delle amministrazioni centrali dello Stato e allo sviluppo del Paese, legge 145/2018”) and of the Space It Up project funded by ASI and the Ministry of University and Research, MUR, under contract n. 2024-5-E.0 CUP n. I53D24000060005.

We thank the technicians (F. Ciancetto, E. Biale, P. Principato) and technologists (M. Prestifilippo) in charge of the INGV-OE camera network. We are also grateful to the volcanologists of INGV-OE who regularly collect data during volcanic events and often work long hours. We would also like to thank the administrative and technical support of INGV-OE that enables us to collect and analyse data.

## DATA AVAILABILITY

All data used to support this study are provided in [Supplementary Material](#) alongside the online version of this article.

## COPYRIGHT NOTICE

© The Author(s) 2026. This article is distributed under the terms of the [Creative Commons Attribution 4.0 International License](#), which permits unrestricted use, distribution, and reproduction in any medium, provided you give appropriate credit to the original author(s) and the source, provide a link to the Creative Commons license, and indicate if changes were made.

## REFERENCES

- Aiuppa, A., M. Bitetto, V. Francofonte, G. Velasquez, C. B. Parra, G. Giudice, M. Liuzzo, R. Moretti, Y. Moussallam, N. Peters, G. Tamburello, O. A. Valderrama, and A. Curtis (2017). “A CO<sub>2</sub>-gas precursor to the March 2015 Villarrica volcano eruption”. *Geochemistry, Geophysics, Geosystems* 18(6), pages 2120–2132. DOI: [10.1002/2017gc006892](https://doi.org/10.1002/2017gc006892).
- Aiuppa, A., G. Giudice, S. Gurrieri, M. Liuzzo, M. Burton, T. Caltabiano, A. J. S. McGonigle, G. Salerno, H. Shinohara, and M. Valenza (2008). “Total volatile flux from Mount Etna”. *Geophysical Research Letters* 35(24). DOI: [10.1029/2008gl035871](https://doi.org/10.1029/2008gl035871).
- Allard, P. (2010). “A CO<sub>2</sub>-rich gas trigger of explosive paroxysms at Stromboli basaltic volcano, Italy”. *Journal of Volcanology and Geothermal Research* 189(3–4), pages 363–374. DOI: [10.1016/j.jvolgeores.2009.11.018](https://doi.org/10.1016/j.jvolgeores.2009.11.018).
- Aloisi, M., A. Bonaccorso, F. Cannavò, and G. M. Currenti (2018). “Coupled Short- and Medium-Term Geophysical Signals at Etna Volcano: Using Deformation and Strain to

- Infer Magmatic Processes From 2009 to 2017". *Frontiers in Earth Science* 6. DOI: [10.3389/feart.2018.00109](https://doi.org/10.3389/feart.2018.00109).
- Alparone, S., D. Andronico, L. Lodato, and T. Sgroi (2003). "Relationship between tremor and volcanic activity during the Southeast Crater eruption on Mount Etna in early 2000". *Journal of Geophysical Research: Solid Earth* 108(B5). DOI: [10.1029/2002jb001866](https://doi.org/10.1029/2002jb001866).
- Alparone, S., D. Andronico, T. Sgroi, F. Ferrari, L. Lodato, and D. Reitano (2007). "Alert system to mitigate tephra fallout hazards at Mt. Etna Volcano, Italy". *Natural Hazards* 43(3), pages 333–350. DOI: [10.1007/s11069-007-9120-7](https://doi.org/10.1007/s11069-007-9120-7).
- Amadio, F., L. Pioli, and S. Scollo (2024). "Constraining proximal grainsize distribution of tephra from paroxysmal eruptions at Etna volcano". *Journal of Volcanology and Geothermal Research* 454, page 108164. DOI: [10.1016/j.jvolgeores.2024.108164](https://doi.org/10.1016/j.jvolgeores.2024.108164).
- Andronico, D., S. Branca, S. Calvari, M. Burton, T. Caltabiano, R. A. Corsaro, P. Del Carlo, G. Garfi, L. Lodato, L. Miraglia, F. Murè, M. Neri, E. Pecora, M. Pompilio, G. Salerno, and L. Spampinato (2005). "A multi-disciplinary study of the 2002/03 Etna eruption: insights into a complex plumbing system". *Bulletin of Volcanology* 67(4), pages 314–330. DOI: [10.1007/s00445-004-0372-8](https://doi.org/10.1007/s00445-004-0372-8).
- Andronico, D., A. Cannata, G. Di Grazia, and F. Ferrari (2021). "The 1986–2021 paroxysmal episodes at the summit craters of Mt. Etna: Insights into volcano dynamics and hazard". *Earth-Science Reviews* 220, page 103686. DOI: [10.1016/j.earscirev.2021.103686](https://doi.org/10.1016/j.earscirev.2021.103686).
- Andronico, D., S. Scollo, M. D. Lo Castro, A. Cristaldi, L. Lodato, and J. Taddeucci (2014). "Eruption dynamics and tephra dispersal from the 24 November 2006 paroxysm at South-East Crater, Mt Etna, Italy". *Journal of Volcanology and Geothermal Research* 274, pages 78–91. DOI: [10.1016/j.jvolgeores.2014.01.009](https://doi.org/10.1016/j.jvolgeores.2014.01.009).
- Behncke, B., M. Neri, E. Pecora, and V. Zanon (2006). "The exceptional activity and growth of the Southeast Crater, Mount Etna (Italy), between 1996 and 2001". *Bulletin of Volcanology* 69(2), pages 149–173. DOI: [10.1007/s00445-006-0061-x](https://doi.org/10.1007/s00445-006-0061-x).
- Bertagnini, A., A. Di Roberto, and M. Pompilio (2011). "Paroxysmal activity at Stromboli: lessons from the past". *Bulletin of Volcanology* 73(9), pages 1229–1243. DOI: [10.1007/s00445-011-0470-3](https://doi.org/10.1007/s00445-011-0470-3).
- Blong, R. J. (1984). *Volcanic hazards: a sourcebook on the effects of eruptions*. Academic Press Australia. 424 pages. ISBN: 0-12-107180-4.
- Bonaccorso, A., T. Caltabiano, G. Currenti, C. Del Negro, S. Gambino, G. Ganci, S. Giammanco, F. Greco, A. Pistorio, G. Salerno, S. Spampinato, and E. Boschi (2011). "Dynamics of a lava fountain revealed by geophysical, geochemical and thermal satellite measurements: The case of the 10 April 2011 Mt Etna eruption: Lava fountain multidisciplinary approach". *Geophysical Research Letters* 38(24). DOI: [10.1029/2011gl049637](https://doi.org/10.1029/2011gl049637).
- Bonaccorso, A., S. Calvari, A. Linde, and S. Sacks (2014). "Eruptive processes leading to the most explosive lava fountain at Etna volcano: The 23 November 2013 episode". *Geophysical Research Letters* 41(14), pages 4912–4919. DOI: [10.1002/2014gl060623](https://doi.org/10.1002/2014gl060623).
- Bonaccorso, A., L. Carleo, G. Currenti, and A. Sicali (2021). "Magma Migration at Shallower Levels and Lava Fountains Sequence as Revealed by Borehole Dilatometers on Etna Volcano". *Frontiers in Earth Science* 9. DOI: [10.3389/feart.2021.740505](https://doi.org/10.3389/feart.2021.740505).
- Bonaccorso, A., G. Currenti, A. Linde, and S. Sacks (2013). "New data from borehole strainmeters to infer lava fountain sources (Etna 2011–2012)". *Geophysical Research Letters* 40(14), pages 3579–3584. DOI: [10.1002/grl.50692](https://doi.org/10.1002/grl.50692).
- Bonaccorso, A., S. D'Amico, M. Mattia, and D. Patanè (2004). "Intrusive Mechanisms at Mt. Etna Forerunning the July–August 2001 Eruption from Seismic and Ground Deformation Data". *Pure and Applied Geophysics* 161(7), pages 1469–1487. DOI: [10.1007/s00024-004-2515-4](https://doi.org/10.1007/s00024-004-2515-4).
- Bonforte, A., A. Bonaccorso, F. Guglielmino, M. Palano, and G. Puglisi (2008). "Feeding system and magma storage beneath Mt. Etna as revealed by recent inflation/deflation cycles". *Journal of Geophysical Research: Solid Earth* 113(B5). DOI: [10.1029/2007jb005334](https://doi.org/10.1029/2007jb005334).
- Calvari, S., G. Bilotta, A. Bonaccorso, T. Caltabiano, A. Cappello, C. Corradino, C. Del Negro, G. Ganci, M. Neri, E. Pecora, G. G. Salerno, and L. Spampinato (2020). "The VEI 2 Christmas 2018 Etna Eruption: A Small But Intense Eruptive Event or the Starting Phase of a Larger One?" *Remote Sensing* 12(6), page 905. DOI: [10.3390/rs12060905](https://doi.org/10.3390/rs12060905).
- Calvari, S., A. Bonaccorso, and G. Ganci (2021). "Anatomy of a Paroxysmal Lava Fountain at Etna Volcano: The Case of the 12 March 2021, Episode". *Remote Sensing* 13(15), page 3052. DOI: [10.3390/rs13153052](https://doi.org/10.3390/rs13153052).
- Calvari, S. and G. Nunnari (2022). "Comparison between Automated and Manual Detection of Lava Fountains from Fixed Monitoring Thermal Cameras at Etna Volcano, Italy". *Remote Sensing* 14(10), page 2392. DOI: [10.3390/rs14102392](https://doi.org/10.3390/rs14102392).
- Calvari, S., G. G. Salerno, L. Spampinato, M. Gouhier, A. La Spina, E. Pecora, A. J. L. Harris, P. Labazuy, E. Biale, and E. Boschi (2011). "An unloading foam model to constrain Etna's 11–13 January 2011 lava fountaining episode: The 11–13 Jan 2011 Etna's lava fountain". *Journal of Geophysical Research: Solid Earth* 116(B11). DOI: [10.1029/2011jb008407](https://doi.org/10.1029/2011jb008407).
- Cannata, A., G. Di Grazia, M. Giuffrida, S. Gresta, M. Palano, M. Sciotto, M. Viccaro, and F. Zuccarello (2018). "Space-Time Evolution of Magma Storage and Transfer at Mt. Etna Volcano (Italy): The 2015–2016 Reawakening of Voragine Crater". *Geochemistry, Geophysics, Geosystems* 19(2), pages 471–495. DOI: [10.1002/2017gc007296](https://doi.org/10.1002/2017gc007296).
- Caricchi, L., C. P. Montagna, A. Aiuppa, J. Lages, G. Tamburillo, and P. Papale (2024). "CO<sub>2</sub> Flushing Triggers Paroxysmal Eruptions at Open Conduit Basaltic Volcanoes". *Journal of Geophysical Research: Solid Earth* 129(4). DOI: [10.1029/2023jb028486](https://doi.org/10.1029/2023jb028486).
- Carr, B. B., E. Lev, T. Sawi, K. A. Bennett, C. S. Edwards, S. A. Soule, S. Vallejo Vargas, and G. I. Marliyani (2021). "Mapping and classification of volcanic deposits using multi-sensor unoccupied aerial systems". *Remote Sensing of En-*

- vironment 264, page 112581. DOI: [10.1016/j.rse.2021.112581](https://doi.org/10.1016/j.rse.2021.112581).
- Casadevall, T. J. (1994). “The 1989–1990 eruption of Redoubt Volcano, Alaska: impacts on aircraft operations”. *Journal of Volcanology and Geothermal Research* 62(1–4), pages 301–316. DOI: [10.1016/0377-0273\(94\)90038-8](https://doi.org/10.1016/0377-0273(94)90038-8).
- Chiarabba, C., A. Amato, E. Boschi, and F. Barberi (2000). “Recent seismicity and tomographic modeling of the Mount Etna plumbing system”. *Journal of Geophysical Research: Solid Earth* 105(B5), pages 10923–10938. DOI: [10.1029/1999jb900427](https://doi.org/10.1029/1999jb900427).
- Collins, S., D. Pyle, and J. Maclennan (2009). “Melt inclusions track pre-eruption storage and dehydration of magmas at Etna”. *Geology* 37(6), pages 571–574. DOI: [10.1130/g30040a.1](https://doi.org/10.1130/g30040a.1).
- Coppola, D., M. Laiolo, C. Cigolini, F. Massimetti, D. Delle Donne, M. Ripepe, H. Arias, S. Barsotti, C. B. Parra, R. G. Centeno, S. Cevuard, G. Chigna, C. Chun, E. Garaebiti, D. Gonzales, J. Griswold, J. Juarez, L. E. Lara, C. M. López, O. Macedo, C. Mahinda, S. Ogburn, O. Prambada, P. Ramon, D. Ramos, A. Peltier, S. Saunders, E. de Zeeuw-van Dalfsen, N. Varley, and R. William (2020). “Thermal Remote Sensing for Global Volcano Monitoring: Experiences From the MIROVA System”. *Frontiers in Earth Science* 7. DOI: [10.3389/feart.2019.00362](https://doi.org/10.3389/feart.2019.00362).
- Corsaro, R. A., D. Andronico, B. Behncke, S. Branca, T. Caltabiano, F. Ciancitto, A. Cristaldi, E. De Beni, A. La Spina, L. Lodato, L. Miraglia, M. Neri, G. Salerno, S. Scollo, and G. Spata (2017). “Monitoring the December 2015 summit eruptions of Mt. Etna (Italy): Implications on eruptive dynamics”. *Journal of Volcanology and Geothermal Research* 341, pages 53–69. DOI: [10.1016/j.jvolgeores.2017.04.018](https://doi.org/10.1016/j.jvolgeores.2017.04.018).
- Corsaro, R., V. Di Renzo, S. Distefano, L. Miraglia, and L. Civetta (2013). “Relationship between petrologic processes in the plumbing system of Mt. Etna and the dynamics of the eastern flank from 1995 to 2005”. *Journal of Volcanology and Geothermal Research* 251, pages 75–89. DOI: [10.1016/j.jvolgeores.2012.02.010](https://doi.org/10.1016/j.jvolgeores.2012.02.010).
- Corsaro, R. A., N. Métrich, P. Allard, D. Andronico, L. Miraglia, and C. Fourmentraux (2009). “The 1974 flank eruption of Mount Etna: An archetype for deep dike-fed eruptions at basaltic volcanoes and a milestone in Etna’s recent history”. *Journal of Geophysical Research: Solid Earth* 114(B7). DOI: [10.1029/2008jb006013](https://doi.org/10.1029/2008jb006013).
- Corsaro, R. A. and L. Miraglia (2022). “Near Real-Time Petrologic Monitoring on Volcanic Glass to Infer Magmatic Processes During the February–April 2021 Paroxysms of the South-East Crater, Etna”. *Frontiers in Earth Science* 10. DOI: [10.3389/feart.2022.828026](https://doi.org/10.3389/feart.2022.828026).
- Corsaro, R. A., L. Miraglia, and M. Pompilio (2007). “Petrologic evidence of a complex plumbing system feeding the July–August 2001 eruption of Mt. Etna, Sicily, Italy”. *Bulletin of Volcanology* 69(4), pages 401–421. DOI: [10.1007/s00445-006-0083-4](https://doi.org/10.1007/s00445-006-0083-4).
- Costantini, L., L. Pioli, C. Bonadonna, J. Clavero, and C. Longchamp (2011). “A Late Holocene explosive mafic eruption of Villarrica volcano, Southern Andes: The Chaimilla deposit”. *Journal of Volcanology and Geothermal Research* 200(3–4), pages 143–158. DOI: [10.1016/j.jvolgeores.2010.12.010](https://doi.org/10.1016/j.jvolgeores.2010.12.010).
- Crozier, J., S. Tramontano, P. Forte, S. J. C. Oliva, H. M. Gonnermann, E. Lev, M. Manga, M. Myers, E. Rader, P. Ruprecht, H. Tuffen, R. Paisley, B. F. Houghton, T. Shea, C. I. Schipper, and J. M. Castro (2022). “Outgassing through magmatic fractures enables effusive eruption of silicic magma”. *Journal of Volcanology and Geothermal Research* 430, page 107617. DOI: [10.1016/j.jvolgeores.2022.107617](https://doi.org/10.1016/j.jvolgeores.2022.107617).
- Currenti, G. and A. Bonaccorso (2019). “Cyclic magma recharge pulses detected by high-precision strainmeter data: the case of 2017 inter-eruptive activity at Etna volcano”. *Scientific Reports* 9(1). DOI: [10.1038/s41598-019-44066-w](https://doi.org/10.1038/s41598-019-44066-w).
- De Angelis, S., L. Zuccarello, S. Scollo, and L. Mereu (2023). “Assessment of eruption source parameters using infrasound and plume modelling: a case study from the 2021 eruption of Mt. Etna, Italy”. *Scientific Reports* 13(1). DOI: [10.1038/s41598-023-46160-6](https://doi.org/10.1038/s41598-023-46160-6).
- De Gori, P., E. Giampiccolo, O. Cocina, S. Branca, C. Doglioni, and C. Chiarabba (2021). “Re-pressurized magma at Mt. Etna, Italy, may feed eruptions for years”. *Communications Earth & Environment* 2(1). DOI: [10.1038/s43247-021-00282-9](https://doi.org/10.1038/s43247-021-00282-9).
- Edwards, M. J. and L. Pioli (2019). “Magma and tephra characteristics for the 17–25 May 2016 Mt Etna eruption”. *Data in Brief* 22, pages 65–71. DOI: [10.1016/j.dib.2018.11.093](https://doi.org/10.1016/j.dib.2018.11.093).
- Edwards, M. J., L. Pioli, D. Andronico, S. Scollo, F. Ferrari, and A. Cristaldi (2018). “Shallow factors controlling the explosivity of basaltic magmas: The 17–25 May 2016 eruption of Etna Volcano (Italy)”. *Journal of Volcanology and Geothermal Research* 357, pages 425–436. DOI: [10.1016/j.jvolgeores.2018.05.015](https://doi.org/10.1016/j.jvolgeores.2018.05.015).
- Farquharson, J. I., M. J. Heap, Y. Lavallée, N. R. Varley, and P. Baud (2016). “Evidence for the development of permeability anisotropy in lava domes and volcanic conduits”. *Journal of Volcanology and Geothermal Research* 323, pages 163–185. DOI: [10.1016/j.jvolgeores.2016.05.007](https://doi.org/10.1016/j.jvolgeores.2016.05.007).
- Ferlito, C. and G. Lanzafame (2010). “The role of supercritical fluids in the potassium enrichment of magmas at Mount Etna volcano (Italy)”. *Lithos* 119(3–4), pages 642–650. DOI: [10.1016/j.lithos.2010.08.006](https://doi.org/10.1016/j.lithos.2010.08.006).
- Gaudin, D., J. Taddeucci, P. Scarlato, E. del Bello, T. Ricci, T. Orr, B. Houghton, A. Harris, S. Rao, and A. Bucci (2017a). “Integrating puffing and explosions in a general scheme for Strombolian-style activity”. *Journal of Geophysical Research: Solid Earth* 122(3), pages 1860–1875. DOI: [10.1002/2016jb013707](https://doi.org/10.1002/2016jb013707).
- Gaudin, D., J. Taddeucci, P. Scarlato, A. Harris, M. Bombrun, E. Del Bello, and T. Ricci (2017b). “Characteristics of puffing activity revealed by ground-based, thermal infrared imaging: the example of Stromboli Volcano (Italy)”. *Bulletin of Volcanology* 79(3). DOI: [10.1007/s00445-017-1108-x](https://doi.org/10.1007/s00445-017-1108-x).
- Giuffrida, M., M. Cardone, F. Zuccarello, and M. Viccaro (2023). “Etna 2011–2022: Discoveries from a decade of activity at the volcano”. *Earth-Science Reviews* 245, page 104563. DOI: [10.1016/j.earscirev.2023.104563](https://doi.org/10.1016/j.earscirev.2023.104563).

- Giuffrida, M. and M. Viccaro (2017). “Three years (2011–2013) of eruptive activity at Mt. Etna: Working modes and timescales of the modern volcano plumbing system from micro-analytical studies of crystals”. *Earth-Science Reviews* 171, pages 289–322. DOI: [10.1016/j.earscirev.2017.06.003](https://doi.org/10.1016/j.earscirev.2017.06.003).
- Gonnermann, H. M. and M. Manga (2007). “The Fluid Mechanics Inside a Volcano”. *Annual Review of Fluid Mechanics* 39(1), pages 321–356. DOI: [10.1146/annurev.fluid.39.050905.110207](https://doi.org/10.1146/annurev.fluid.39.050905.110207).
- Guffanti, M., G. C. Mayberry, T. J. Casadevall, and R. Wunderman (2009). “Volcanic hazards to airports”. *Natural Hazards* 51(2), pages 287–302. DOI: [10.1007/s11069-008-9254-2](https://doi.org/10.1007/s11069-008-9254-2).
- Harris, A. J. L. and S. M. Baloga (2009). “Lava discharge rates from satellite-measured heat flux”. *Geophysical Research Letters* 36(19). DOI: [10.1029/2009gl039717](https://doi.org/10.1029/2009gl039717).
- Harris, A. J. L. and M. Ripepe (2007). “Temperature and dynamics of degassing at Stromboli”. *Journal of Geophysical Research: Solid Earth* 112(B3). DOI: [10.1029/2006jb004393](https://doi.org/10.1029/2006jb004393).
- Houghton, B. F., C. M. Tisdale, E. W. Llewellyn, J. Taddeucci, T. R. Orr, B. Walker, and M. R. Patrick (2021). “The Birth of a Hawaiian Fissure Eruption”. *Journal of Geophysical Research: Solid Earth* 126(1). DOI: [10.1029/2020jb020903](https://doi.org/10.1029/2020jb020903).
- Houghton, B. F., C. J. N. Wilson, P. Del Carlo, M. Coltelli, J. E. Sable, and R. Carey (2004). “The influence of conduit processes on changes in style of basaltic Plinian eruptions: Tarawera 1886 and Etna 122 BC”. *Journal of Volcanology and Geothermal Research* 137(1–3), pages 1–14. DOI: [10.1016/j.jvolgeores.2004.05.009](https://doi.org/10.1016/j.jvolgeores.2004.05.009).
- Jaupart, C. and S. Vergnolle (1989). “The generation and collapse of a foam layer at the roof of a basaltic magma chamber”. *Journal of Fluid Mechanics* 203, pages 347–380. DOI: [10.1017/s0022112089001497](https://doi.org/10.1017/s0022112089001497).
- Johnson, J. B., L. M. Watson, J. L. Palma, E. M. Dunham, and J. F. Anderson (2018). “Forecasting the Eruption of an Open-Vent Volcano Using Resonant Infrasound Tones”. *Geophysical Research Letters* 45(5), pages 2213–2220. DOI: [10.1002/2017gl076506](https://doi.org/10.1002/2017gl076506).
- Kahl, M., S. Chakraborty, F. Costa, and M. Pompilio (2011). “Dynamic plumbing system beneath volcanoes revealed by kinetic modeling, and the connection to monitoring data: An example from Mt. Etna”. *Earth and Planetary Science Letters* 308(1–2), pages 11–22. DOI: [10.1016/j.epsl.2011.05.008](https://doi.org/10.1016/j.epsl.2011.05.008).
- Kahl, M., S. Chakraborty, M. Pompilio, and F. Costa (2015). “Constraints on the Nature and Evolution of the Magma Plumbing System of Mt. Etna Volcano (1991–2008) from a Combined Thermodynamic and Kinetic Modelling of the Compositional Record of Minerals”. *Journal of Petrology* 56(10), pages 2025–2068. DOI: [10.1093/petrology/egv063](https://doi.org/10.1093/petrology/egv063).
- Leduc, L., L. Gurioli, A. Harris, L. Colò, and E. F. Rose-Koga (2015). “Types and mechanisms of strombolian explosions: characterization of a gas-dominated explosion at Stromboli”. *Bulletin of Volcanology* 77(1). DOI: [10.1007/s00445-014-0888-5](https://doi.org/10.1007/s00445-014-0888-5).
- Liu, E. J., K. V. Cashman, E. Miller, H. Moore, M. Edmonds, B. E. Kunz, F. Jenner, and G. Chigna (2020). “Petrologic monitoring at Volcán de Fuego, Guatemala”. *Journal of Volcanology and Geothermal Research* 405, page 107044. DOI: [10.1016/j.jvolgeores.2020.107044](https://doi.org/10.1016/j.jvolgeores.2020.107044).
- Marzano, F. S., L. Mereu, S. Scollo, F. Donnadieu, and C. Bonadonna (2020). “Tephra Mass Eruption Rate From Ground-Based X-Band and L-Band Microwave Radars During the November 23, 2013, Etna Paroxysm”. *IEEE Transactions on Geoscience and Remote Sensing* 58(5), pages 3314–3327. DOI: [10.1109/tgrs.2019.2953167](https://doi.org/10.1109/tgrs.2019.2953167).
- Mastin, L., M. Guffanti, R. Servranckx, P. Webley, S. Barsotti, K. Dean, A. Durant, J. Ewert, A. Neri, W. Rose, D. Schneider, L. Siebert, B. Stunder, G. Swanson, A. Tupper, A. Volentik, and C. Waythomas (2009). “A multidisciplinary effort to assign realistic source parameters to models of volcanic ash-cloud transport and dispersion during eruptions”. *Journal of Volcanology and Geothermal Research* 186(1–2), pages 10–21. DOI: [10.1016/j.jvolgeores.2009.01.008](https://doi.org/10.1016/j.jvolgeores.2009.01.008).
- Mereu, L., F. S. Marzano, M. Montopoli, and C. Bonadonna (2015). “Retrieval of Tephra Size Spectra and Mass Flow Rate From C-Band Radar During the 2010 Eyjafjallajökull Eruption, Iceland”. *IEEE Transactions on Geoscience and Remote Sensing* 53(10), pages 5644–5660. DOI: [10.1109/tgrs.2015.2427032](https://doi.org/10.1109/tgrs.2015.2427032).
- Mereu, L., F. S. Marzano, S. Scollo, M. Montopoli, and G. Vulpani (2024). “Volcanic plume retrieval using weather radar”. *Advances in Weather Radar. Volume 3: Emerging applications*. Edited by V. Bringi, K. V. Mishra, and M. Thurai. Volume 3. Institution of Engineering and Technology. Chapter 4, pages 129–160. ISBN: 9781839536267. DOI: [10.1049/sbra557h\\_ch4](https://doi.org/10.1049/sbra557h_ch4).
- Mereu, L., S. Scollo, C. Bonadonna, F. Donnadieu, V. Freret-Lorgeril, and F. S. Marzano (2022). “Ground-Based Remote Sensing and Uncertainty Analysis of the Mass Eruption Rate Associated With the 3–5 December 2015 Paroxysms of Mt. Etna”. *IEEE Journal of Selected Topics in Applied Earth Observations and Remote Sensing* 15, pages 504–518. DOI: [10.1109/jstars.2021.3133946](https://doi.org/10.1109/jstars.2021.3133946).
- Mereu, L., S. Scollo, C. Bonadonna, V. Freret-Lorgeril, and F. S. Marzano (2020). “Multisensor Characterization of the Incandescent Jet Region of Lava Fountain-Fed Tephra Plumes”. *Remote Sensing* 12(21), page 3629. DOI: [10.3390/rs12213629](https://doi.org/10.3390/rs12213629).
- Mereu, L., S. Scollo, A. Garcia, L. Sandri, C. Bonadonna, and F. S. Marzano (2023). “A New Radar-Based Statistical Model to Quantify Mass Eruption Rate of Volcanic Plumes”. *Geophysical Research Letters* 50(7). DOI: [10.1029/2022gl100596](https://doi.org/10.1029/2022gl100596).
- Mereu, L., M. Stocchi, A. Garcia, M. Prestifilippo, L. Sandri, C. Bonadonna, and S. Scollo (2025). “Estimating the mass of tephra accumulated on roads to best manage the impact of volcanic eruptions: the example of Mt Etna, Italy”. *Natural Hazards and Earth System Sciences* 25(6), pages 1943–1962. DOI: [10.5194/nhess-25-1943-2025](https://doi.org/10.5194/nhess-25-1943-2025).
- Métrich, N., P. Allard, N. Spilliaert, D. Andronico, and M. Burton (2004). “2001 flank eruption of the alkali- and volatile-rich primitive basalt responsible for Mount Etna’s evolution

- in the last three decades”. *Earth and Planetary Science Letters* 228(1–2), pages 1–17. DOI: [10.1016/j.epsl.2004.09.036](https://doi.org/10.1016/j.epsl.2004.09.036).
- Métrich, N., A. Bertagnini, and M. Pistolesi (2021). “Paroxysms at Stromboli Volcano (Italy): Source, Genesis and Dynamics”. *Frontiers in Earth Science* 9. DOI: [10.3389/feart.2021.593339](https://doi.org/10.3389/feart.2021.593339).
- Montopoli, M., G. Ferrauto, D. Scaranari, S. Barbieri, M. Biscarini, V. Capozzi, L. Mereu, M. T. Falconi, R. Ferretti, and G. Vulpiani (2023). “Overview on Weather Radar Applications”. *2023 17th European Conference on Antennas and Propagation (EuCAP)*. IEEE, pages 1–5. DOI: [10.23919/eucap57121.2023.10133034](https://doi.org/10.23919/eucap57121.2023.10133034).
- Murru, M., C. Montuori, M. Wyss, and E. Privitera (1999). “The locations of magma chambers at Mt. Etna, Italy, mapped by b-values”. *Geophysical Research Letters* 26(16), pages 2553–2556. DOI: [10.1029/1999gl1900568](https://doi.org/10.1029/1999gl1900568).
- Naismith, A. K., I. Matthew Watson, R. Escobar-Wolf, G. Chigna, H. Thomas, D. Coppola, and C. Chun (2019). “Eruption frequency patterns through time for the current (1999–2018) activity cycle at Volcán de Fuego derived from remote sensing data: Evidence for an accelerating cycle of explosive paroxysms and potential implications of eruptive activity”. *Journal of Volcanology and Geothermal Research* 371, pages 206–219. DOI: [10.1016/j.jvolgeores.2019.01.001](https://doi.org/10.1016/j.jvolgeores.2019.01.001).
- Newhall, C., F. Costa, A. Ratdomopurbo, D. Venezky, C. Widuwijayanti, N. T. Z. Win, K. Tan, and E. Fajiculay (2017). “WOVOdat – An online, growing library of worldwide volcanic unrest”. *Journal of Volcanology and Geothermal Research* 345, pages 184–199. DOI: [10.1016/j.jvolgeores.2017.08.003](https://doi.org/10.1016/j.jvolgeores.2017.08.003).
- Palano, M., G. Pezzo, and C. Chiarabba (2024). “Magma budget, plutonic growth and lateral spreading at Mt. Etna”. *Communications Earth & Environment* 5(1). DOI: [10.1038/s43247-024-01267-0](https://doi.org/10.1038/s43247-024-01267-0).
- Pallister, J. and S. R. McNutt (2015). “Synthesis of Volcano Monitoring”. *The Encyclopedia of Volcanoes*. Elsevier, pages 1151–1171. ISBN: 9780123859389. DOI: [10.1016/b978-0-12-385938-9.00066-3](https://doi.org/10.1016/b978-0-12-385938-9.00066-3).
- Paonita, A., M. Liuzzo, G. Salerno, C. Federico, P. Bonfanti, A. Caracausi, G. Giuffrida, A. La Spina, T. Caltabiano, S. Guerrieri, and G. Giudice (2021). “Intense overpressurization at basaltic open-conduit volcanoes as inferred by geochemical signals: The case of the Mt. Etna December 2018 eruption”. *Science Advances* 7(36). DOI: [10.1126/sciadv.abg6297](https://doi.org/10.1126/sciadv.abg6297).
- Patanè, D., C. Chiarabba, O. Cocina, P. De Gori, M. Moretti, and E. Boschi (2002). “Tomographic images and 3D earthquake locations of the seismic swarm preceding the 2001 Mt. Etna eruption: Evidence for a dyke intrusion”. *Geophysical Research Letters* 29(10). DOI: [10.1029/2001gl1014391](https://doi.org/10.1029/2001gl1014391).
- Patanè, D., P. De Gori, C. Chiarabba, and A. Bonaccorso (2003). “Magma Ascent and the Pressurization of Mount Etna’s Volcanic System”. *Science* 299(5615), pages 2061–2063. DOI: [10.1126/science.1080653](https://doi.org/10.1126/science.1080653).
- Patrick, M. R., A. J. L. Harris, M. Ripepe, J. Dehn, D. A. Rothery, and S. Calvari (2007). “Strombolian explosive styles and source conditions: insights from thermal (FLIR) video”. *Bulletin of Volcanology* 69(7), pages 769–784. DOI: [10.1007/s00445-006-0107-0](https://doi.org/10.1007/s00445-006-0107-0).
- Polacci, M., R. A. Corsaro, and D. Andronico (2006). “Coupled textural and compositional characterization of basaltic scoria: Insights into the transition from Strombolian to fire fountain activity at Mount Etna, Italy”. *Geology* 34(3), page 201. DOI: [10.1130/g22318.1](https://doi.org/10.1130/g22318.1).
- Prata, F., S. Corradini, R. Biondi, L. Guerrieri, L. Merucci, A. Prata, and D. Stelitano (2024). “Applications of Ground-Based Infrared Cameras for Remote Sensing of Volcanic Plumes”. *Geosciences* 14(3), page 82. DOI: [10.3390/geosciences14030082](https://doi.org/10.3390/geosciences14030082).
- Proietti, C., E. De Beni, M. Cantarero, T. Ricci, and G. Ganci (2023). “Rapid provision of maps and volcanological parameters: quantification of the 2021 Etna volcano lava flows through the integration of multiple remote sensing techniques”. *Bulletin of Volcanology* 85(10). DOI: [10.1007/s00445-023-01673-w](https://doi.org/10.1007/s00445-023-01673-w).
- Puglisi, G., A. Bonforte, A. Ferretti, F. Guglielmino, M. Palano, and C. Prati (2008). “Dynamics of Mount Etna before, during, and after the July–August 2001 eruption inferred from GPS and differential synthetic aperture radar interferometry data”. *Journal of Geophysical Research: Solid Earth* 113(B6). DOI: [10.1029/2006jb004811](https://doi.org/10.1029/2006jb004811).
- Queißer, M., M. Burton, N. Theys, F. Pardini, G. Salerno, T. Caltabiano, M. Varnam, B. Esse, and R. Kazahaya (2019). “TROPOMI enables high resolution SO<sub>2</sub> flux observations from Mt. Etna, Italy, and beyond”. *Scientific Reports* 9(1). DOI: [10.1038/s41598-018-37807-w](https://doi.org/10.1038/s41598-018-37807-w).
- Ripepe, M., E. Marchetti, D. Delle Donne, R. Genco, L. Innocenti, G. Lacanna, and S. Valade (2018). “Infrasonic Early Warning System for Explosive Eruptions”. *Journal of Geophysical Research: Solid Earth* 123(11), pages 9570–9585. DOI: [10.1029/2018jb015561](https://doi.org/10.1029/2018jb015561).
- Ripepe, M., E. Marchetti, G. Ulivieri, A. Harris, J. Dehn, M. Burton, T. Caltabiano, and G. Salerno (2005). “Effusive to explosive transition during the 2003 eruption of Stromboli volcano”. *Geology* 33(5), page 341. DOI: [10.1130/g21173.1](https://doi.org/10.1130/g21173.1).
- Romero, J. E., F. Vera, M. Polacci, D. Morgavi, F. Arzilli, M. A. Alam, J. E. Bustillos, A. Guevara, J. B. Johnson, J. L. Palma, M. Burton, E. Cuenca, and W. Keller (2018). “Tephra From the 3 March 2015 Sustained Column Related to Explosive Lava Fountain Activity at Volcán Villarrica (Chile)”. *Frontiers in Earth Science* 6. DOI: [10.3389/feart.2018.00098](https://doi.org/10.3389/feart.2018.00098).
- Sansivero, F. and G. Vilardo (2019). “Processing Thermal Infrared Imagery Time-Series from Volcano Permanent Ground-Based Monitoring Network. Latest Methodological Improvements to Characterize Surface Temperatures Behavior of Thermal Anomaly Areas”. *Remote Sensing* 11(5), page 553. DOI: [10.3390/rs11050553](https://doi.org/10.3390/rs11050553).
- Scollo, S., S. Tarantola, C. Bonadonna, M. Coltelli, and A. Saltelli (2008). “Sensitivity analysis and uncertainty estimation for tephra dispersal models”. *Journal of Geophysical Research: Solid Earth* 113(B6). DOI: [10.1029/2006jb004864](https://doi.org/10.1029/2006jb004864).
- Simons, B. C., S. J. Cronin, J. D. Eccles, M. S. Bebbington, and A. D. Jolly (2020a). “Spatiotemporal variations in eruption style, magnitude and vent morphology at Yasur volcano,

- Vanuatu: insights into the conduit system". *Bulletin of Volcanology* 82(8). DOI: [10.1007/s00445-020-01394-4](https://doi.org/10.1007/s00445-020-01394-4).
- Simons, B. C., A. D. Jolly, J. D. Eccles, and S. J. Cronin (2020b). "Spatiotemporal Relationships between Two Closely-spaced Strombolian-style Vents, Yasur, Vanuatu". *Geophysical Research Letters* 47(5). DOI: [10.1029/2019gl085687](https://doi.org/10.1029/2019gl085687).
- Spampinato, L., M. Scotto, A. Cannata, F. Cannavò, A. La Spina, M. Palano, G. G. Salerno, E. Privitera, and T. Caltabiano (2015). "Multiparametric study of the February–April 2013 paroxysmal phase of Mt. Etna New South-East crater". *Geochemistry, Geophysics, Geosystems* 16(6), pages 1932–1949. DOI: [10.1002/2015gc005795](https://doi.org/10.1002/2015gc005795).
- Spampinato, S., H. Langer, A. Messina, and S. Falsaperla (2019). "Short-term detection of volcanic unrest at Mt. Etna by means of a multi-station warning system". *Scientific Reports* 9(1). DOI: [10.1038/s41598-019-42930-3](https://doi.org/10.1038/s41598-019-42930-3).
- Sparks, R. S. J., J. Biggs, and J. W. Neuberg (2012). "Monitoring Volcanoes". *Science* 335(6074), pages 1310–1311. DOI: [10.1126/science.1219485](https://doi.org/10.1126/science.1219485).
- Spilliaert, N., P. Allard, N. Métrich, and A. V. Sobolev (2006a). "Melt inclusion record of the conditions of ascent, degassing, and extrusion of volatile-rich alkali basalt during the powerful 2002 flank eruption of Mount Etna (Italy)". *Journal of Geophysical Research: Solid Earth* 111(B4). DOI: [10.1029/2005jb003934](https://doi.org/10.1029/2005jb003934).
- Spilliaert, N., N. Métrich, and P. Allard (2006b). "S–Cl–F degassing pattern of water-rich alkali basalt: Modelling and relationship with eruption styles on Mount Etna volcano". *Earth and Planetary Science Letters* 248(3–4), pages 772–786. DOI: [10.1016/j.epsl.2006.06.031](https://doi.org/10.1016/j.epsl.2006.06.031).
- Swanson, D. A., T. R. Rose, A. E. Mucek, M. O. Garcia, R. S. Fiske, and L. G. Mastin (2014). "Cycles of explosive and effusive eruptions at Kilauea Volcano, Hawaii". *Geology* 42(7), pages 631–634. DOI: [10.1130/g35701.1](https://doi.org/10.1130/g35701.1).
- Taddeucci, J., M. Edmonds, B. Houghton, M. R. James, and S. Vergnolle (2015a). "Hawaiian and Strombolian Eruptions". *The Encyclopedia of Volcanoes*. Elsevier, pages 485–503. ISBN: 9780123859389. DOI: [10.1016/b978-0-12-385938-9.00027-4](https://doi.org/10.1016/b978-0-12-385938-9.00027-4).
- (2015b). "Hawaiian and Strombolian Eruptions". *The Encyclopedia of Volcanoes*. Edited by H. Sigurdsson. Elsevier. Chapter 27, pages 485–503. ISBN: 9780123859389. DOI: [10.1016/b978-0-12-385938-9.00027-4](https://doi.org/10.1016/b978-0-12-385938-9.00027-4).
- Tilling, R. I. (1987). "Introduction to Special Section on How Volcanoes Work: Part 1". *Journal of Geophysical Research: Solid Earth* 92(B13), pages 13685–13686. DOI: [10.1029/jb092ib13p13685](https://doi.org/10.1029/jb092ib13p13685).
- Trusdell, F. A., J. D. Hungerford, J. O. Stone, K. Fifield, K. McCann, H. Wershow, S. Zaarur, and M. D. Boyd (2019). "Explosive eruptions at the summit of Mauna Loa: Lithology, modeling, and dating". *Field Volcanology: A Tribute to the Distinguished Career of Don Swanson*. Edited by M. P. Poland, M. O. Garcia, V. E. Camp, and A. Grunder. Volume 538. Geological Society of America. Chapter 15, pages 325–349. ISBN: 9780813795386. DOI: [10.1130/2018.2538\(15\)](https://doi.org/10.1130/2018.2538(15)).
- Viccaro, M., R. Calcagno, I. Garozzo, M. Giuffrida, and E. Nicotra (2015). "Continuous magma recharge at Mt. Etna during the 2011–2013 period controls the style of volcanic activity and compositions of erupted lavas". *Mineralogy and Petrology* 109(1), pages 67–83. DOI: [10.1007/s00710-014-0352-4](https://doi.org/10.1007/s00710-014-0352-4).
- Viccaro, M., M. Giuffrida, F. Zuccarello, M. Scandura, M. Palano, and S. Gresta (2019). "Violent paroxysmal activity drives self-feeding magma replenishment at Mt. Etna". *Scientific Reports* 9(1). DOI: [10.1038/s41598-019-43211-9](https://doi.org/10.1038/s41598-019-43211-9).
- Vulpiani, G., M. Ripepe, and S. Valade (2016). "Mass discharge rate retrieval combining weather radar and thermal camera observations". *Journal of Geophysical Research: Solid Earth* 121(8), pages 5679–5695. DOI: [10.1002/2016jb013191](https://doi.org/10.1002/2016jb013191).
- Walker, B. H., B. F. Houghton, and E. W. Llewellyn (2023). "Coexisting Strombolian and Hawaiian activity during the 2018 fissure eruption of Kilauea – Implications for processes of weak explosions". *Journal of Volcanology and Geothermal Research* 435, page 107754. DOI: [10.1016/j.jvolgeores.2023.107754](https://doi.org/10.1016/j.jvolgeores.2023.107754).
- Williams-Jones, G. and H. Rymer (2015). "Hazards of Volcanic Gases". *The Encyclopedia of Volcanoes*. Elsevier, pages 985–992. ISBN: 9780123859389. DOI: [10.1016/b978-0-12-385938-9.00057-2](https://doi.org/10.1016/b978-0-12-385938-9.00057-2).
- Wilson, L. and J. W. Head (1981). "Ascent and eruption of basaltic magma on the Earth and Moon". *Journal of Geophysical Research: Solid Earth* 86(B4), pages 2971–3001. DOI: [10.1029/jb086ib04p02971](https://doi.org/10.1029/jb086ib04p02971).
- Zuccarello, F., D. Andronico, P. Del Carlo, M. de' Michieli Vitturi, A. Di Roberto, G. Ganci, B. Behncke, T. Esposti Ongaro, F. Ciancitto, and A. Cappello (2025). "Trigger mechanism and propagation dynamics of pyroclastic density currents at basaltic volcanoes". *Communications Earth & Environment* 6(1). DOI: [10.1038/s43247-025-02397-9](https://doi.org/10.1038/s43247-025-02397-9).